The FEBS Journal

FEBS PRESS science publishing by scientists

EDITOR'S CHOICE

Dynamic control of RSK complexes by phosphoswitch-based regulation

Gergő Gógl[1,2], Beáta Biri-Kovács[1], Ádám L. Póti[2], Henrietta Vadászi[1], Bálint Szeder[2], Andrea Bodor[3], Gitta Schlosser[4], András Ács[5], Lilla Turiák[5], László Buday[2], Anita Alexa[2], László Nyitray[1] and Attila Reményi[2]

1 Department of Biochemistry, ELTE Eötvös Loránd University, Budapest, Hungary
2 Institute of Enzymology, Research Center for Natural Sciences, Hungarian Academy of Sciences, Budapest, Hungary
3 Laboratory of Structural Chemistry and Biology, Institute of Chemistry, ELTE Eötvös Loránd University, Budapest, Hungary
4 MTA-ELTE Research Group of Peptide Chemistry, Hungarian Academy of Sciences, ELTE Eötvös Loránd University, Budapest, Hungary
5 MS Proteomics Research Group, Research Center for Natural Sciences, Hungarian Academy of Sciences, Budapest, Hungary

Keywords
extracellular signal–regulated kinase; linear-binding motif; mitogen-activated kinases; PDZ domain; protein phosphorylation; signal transduction

Correspondence
L. Nyitray, Department of Biochemistry, ELTE Eötvös Loránd University, Budapest, Hungary
Fax: +36 13812172
Tel: +36 13812171
E-mail: nyitray@elte.hu
and
A. Reményi, Institute of Enzymology, Research Center for Natural Sciences, Hungarian Academy of Sciences, Budapest, Hungary
Fax: +36 13826297
Tel: +36 13826613
E-mail: remenyi.attila@ttk.mta.hu

(Received 6 September 2017, revised 18 October 2017, accepted 25 October 2017)

doi:10.1111/febs.14311

Assembly and disassembly of protein–protein complexes needs to be dynamically controlled and phosphoswitches based on linear motifs are crucial in this process. Extracellular signal–regulated kinase 2 (ERK2) recognizes a linear-binding motif at the C-terminal tail (CTT) of ribosomal S6 kinase 1 (RSK1), leading to phosphorylation and subsequent activation of RSK1. The CTT also contains a classical PDZ domain-binding motif which binds RSK substrates (e.g. MAGI-1). We show that autophosphorylation of the disordered CTT promotes the formation of an intramolecular charge clamp, which efficiently masks critical residues and indirectly hinders ERK binding. Thus, RSK1 CTT operates as an autoregulated phosphoswitch: its phosphorylation at specific sites affects its protein-binding capacity and its conformational dynamics. These biochemical feedbacks, which form the structural basis for the rapid dissociation of ERK2-RSK1 and RSK1-PDZ substrate complexes under sustained epidermal growth factor (EGF) stimulation, were structurally characterized and validated in living cells. Overall, conformational changes induced by phosphorylation in disordered regions of protein kinases, coupled to allosteric events occurring in the kinase domain cores, may provide mechanisms that contribute to the emergence of complex signaling activities. In addition, we show that phosphoswitches based on linear motifs can be functionally classified as ON and OFF protein–protein interaction switches or dimmers, depending on the specific positioning of phosphorylation target sites in relation to functional linear-binding motifs. Moreover, interaction of phosphorylated residues with positively charged residues in disordered regions is likely to be a common mechanism of phosphoregulation.

Database
Structural data are available in the PDB database under the accession numbers 5N7D, 5N7F and 5N7G. NMR spectral assignation data are available in the BMRB database under the accession numbers 27213 and 27214.

Abbreviations
ANXA2, annexin A2; CD, common docking; CTKD, C-terminal kinase domain; CTT, C-terminal tail; EGF, epidermal growth factor; ERK2, extracellular signal–regulated kinase 2; HPV, human papillomavirus; ITC, isothermal calorimetry; MAGI-1, membrane-associated guanylate kinase with inverted domain structure protein 1; MAPKAPK, MAPK-activated protein kinase; MAPK, mitogen activated kinase; MD, molecular dynamics; NTKD, N-terminal kinase domain; PDK1, phosphoinositide-dependent kinase 1; RSK1, ribosomal S6 kinase 1; SCS, secondary chemical shifts.

Introduction

Regulation of cellular physiology is based on dynamic protein networks: the activity of network components and their protein–protein interaction capacity are continuously changing depending on extracellular stimuli. Protein phosphorylation is often used as a mechanism by which protein complex activity and assembly could be directly affected [1]. For example, mitogen-activated kinases (MAPK) involved in the regulation of cell growth, death or differentiation form complexes with their partner proteins that are dependent on signaling pathway activation [2]. Interestingly, protein–protein interactions relevant for signaling, particularly those mediated by protein kinases, are mediated by so-called linear motifs. These protein regions do not adopt a well-defined three-dimensional structure on their own [3,4]. Although the role of protein phosphorylation occurring in specific regions of a structured domain could be well-explained by allosteric mechanisms, for linear motif-based interactions, this is not that well-explored [5]. Linear-binding motifs may change their protein-binding capacity upon phosphorylation, but mechanistic insights into how these 'phosphoswitches' affect protein network level modalities (e.g. signaling amplitude or dynamics) are still lacking. Intriguingly, the Ras/ERK cell growth promoting pathway – activated by epidermal growth factor (EGF) – displays interesting dynamic properties [6,7]. However, the molecular principles and the structural basis of rapid biochemical feedbacks, which do not involve transcriptional level regulation and are normally dependent on fast post-translational modifications, are not well-understood.

RSK1 is a member of the MAPK-activated protein kinase (MAPKAPK) family and is one of the downstream effector kinases of the Ras/ERK signaling pathway whose activity is directly controlled by extracellular signal–regulated kinases (ERK) [8]. RSKs contain two kinase domains: a C-terminal regulatory (CAMK-type) kinase domain (CTKD) and an N-terminal effector (AGC-type) kinase domain (NTKD) [9] (Fig. 1A). ERK2 forms a complex with RSK1 in which the activation loop of the CTKD becomes phosphorylated at Thr573 [10]. Importantly, there is an autophosphorylation site at the RSK1 CTT (Ser732), which has a role in the dissociation of the ERK–RSK binary complex [11]. The activated CTKD of RSK1 autophosphorylates the linker connecting the two kinase domains at Ser380, recruiting phosphoinositide-dependent kinase 1 (PDK1), which then phosphorylates the activation loop of NTKD at Ser221 [12]. Ultimately, the activated NTKD will phosphorylate RSK substrates.

The C terminus of RSK contains multiple overlapping linear motifs: in addition to the ERK-binding site (often referred to as a MAPK docking motif) and its own autophosphorylation site, the calcium-binding S100B protein also binds to the CTT [13] (Fig. 1B). The N-terminal part of the CTT contains the inhibitory segment (696–709) that adopts a helical conformation and blocks the CTKD substrate-binding pocket [14]. ERK phosphorylation at the CTKD activation loop renders this inhibitory segment disordered, but this likely does not influence the tight binding of ERK2 to RSK1 ($K_D \approx 0.1$ μM) [10,15] (Fig. 1C).

The last residues of RSKs contain a structurally uncharacterized class I PDZ substrate motif (class I consensus motif: X[ST]X[VL]) that also contains the Ser732 autophosphorylation site (Fig. 1C). RSK2 was previously identified as a PDZ-binding partner of scaffold/anchor proteins (Shank1, MAGI-1, GRIP, and SNX27), which may all get phosphorylated by the recruited kinase [16,17]. Similarly, RSK1 also has two known PDZ-binding partners (MAGI-1 and EBP50) [16,18]. Some of these proteins (e.g. Shank and EBP50) were indeed shown to be RSK substrates, but there are many putative RSK phosphorylation sites in other binding partners as well. RSK substrates without PDZ domains usually overlap with other AGC kinase substrates; therefore, RSK seems to be a relatively low specificity kinase [19]. Since PDZ containing substrates specifically interact with RSKs, they could represent a highly specific RSK phosphorylation target group and these interactions could also be important in the precise subcellular trafficking of RSK1.

Membrane-associated guanylate kinase with inverted domain structure proteins (MAGI) are nuclear or tight junction-associated scaffolds and RSK substrate proteins with tumor suppressor functions [20]. MAGI-3 was shown to be a regulator of the β2-adrenergic receptor or lysophosphatidic acid induced ERK2 activation [21,22]. All MAGI proteins contain six PDZ domains, two WW domains and an inactive guanylate kinase domain. RSK was shown to be an interaction partner of the second PDZ domain of MAGI-1. This PDZ domain is one of the few domains that may prefer Leu at the C terminus from the class I group with an optimal sequence of RxxTLL [23]. Moreover, there are seven identified phosphosites in the C-terminal tail of MAGI-1 conferring to a RSK AGC kinase-type phosphorylation consensus motif ([RK]xRxx[ST]) [24,25].

Here, we demonstrate the regulated and dynamic nature of ERK2–RSK1 and RSK1–MAGI-1 complexes in live cells following Ras/ERK signaling pathway stimulation. Autophosphorylation, PDZ, and MAPK binding all target the 40-residue-long, disordered C-terminal tail of RSK1, and our findings are in good agreement with

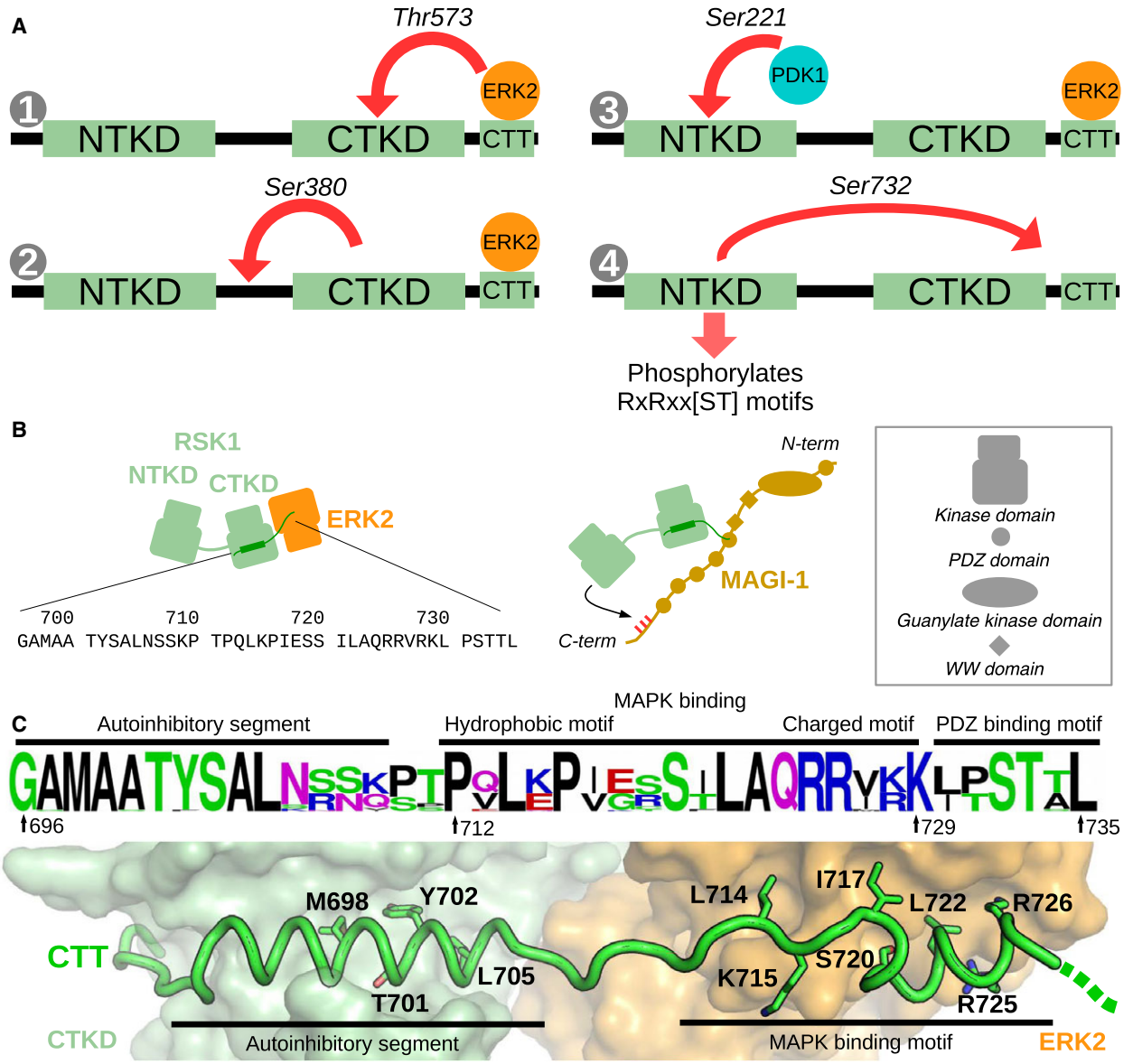

Fig. 1. Overview of RSK1, ERK2, and MAGI-1 proteins and their complexes. (A) Schematic RSK1 activation mechanism. The 4-step activation mechanism involves (1) phosphorylation by ERK, (2) CTKD autophosphorylation, (3) association and activation by PDK1, and (4) NTKD autophosphorylation which remodels the ERK-binding tail. (B) Schematic representation and domain architecture of RSK1, ERK2, and MAGI-1 and their binary complexes. The putative RSK1 phosphorylation sites in MAGI-1 are marked by red. The sequence of the C-terminal tail (CTT) of human RSK1 is also indicated. (C) Evolutionary conservation profile of vertebrate RSK1/RSK2 CTT sequences. Functional regions and peptide boundaries are highlighted. In the lower panel, the ERK2 bound state of RSK1 is presented where important residues are shown by stick representation (PDB ID: 4NIF). The conserved last seven residues of RSK1 is invisible in this crystal structure.

the decreased ERK2-binding capacity of RSK1 observed after Ras/ERK pathway activation in cells [11]. In summary, our results provide a biochemical and structural basis underlying ERK signaling dynamics and feedback mechanisms: Ras-ERK pathway activation influences RSK-PDZ substrate interaction and activator MAP kinase binding by using an autoregulatory phosphoswitch located in the disordered RSK C-terminal tail.

Results

In vitro phosphorylation of full-length RSK1

Activated ERK phosphorylates RSK1 at specific sites triggering a hierarchical set of further phosphorylation events involving both kinase domains of RSK and PDK1, which will ultimately promote cell growth. In order to clarify the

role of individual phosphorylation events, we first investigated the *in vitro* phosphorylation pattern of RSK1 under controlled conditions. We produced recombinant full-length RSK1 (FL-RSK1), active ERK2, and PDK1 kinases. RSK1 or a mixture of RSK1 and upstream kinases were incubated in the presence of ATP, and then we searched for RSK1 phosphopeptides using mass spectrometry (MS). We could reproduce most known phosphorylation sites [24,26] (Fig. 2A). All major phosphosites can be associated with the complex activation mechanism of RSK1 except for the C-terminal autophosphorylation sites. Here, Ser732 was the main phosphorylated site, but we could also detect both Thr733 and Thr734 phosphorylated peptides. These latter CTT autophosphorylation sites might be mutually exclusive because no double or triple phosphorylated peptides were observed.

Since autophosphorylation of the CTT had been formerly attributed to the activity of the NTKD [11,12], we wanted to further clarify the role of the CTKD as our data indicated this enzymatic domain to be important for CTT phosphorylation. We constructed a constitutively active CTKD by introducing a phospho-mimicking mutation into the activation loop (T573E mutation). In kinase assays where the phosphorylation of a RSK1 substrate peptide (containing the phosphosite Ser380) was monitored *in trans*, autophosphorylation of the CTKD was also prominent (Fig. 2B). Further MS analysis identified that Ser732 was highly phosphorylated in this sample. We were also able to phosphorylate isolated C-terminal RSK1 peptides with the same construct, where again Ser732 was phosphorylated selectively (Fig. 2C). In conclusion, we provide evidence that the C-terminal autophosphorylation site (Ser732) of RSK1 is preferentially phosphorylated by the CTKD and not by the NTKD.

RSK1 binds to the second PDZ domain of MAGI-1 via its C terminus

Next, we wanted to address the biochemical relevance of Ser732 autophosphorylation, particularly in terms of RSK-partner protein binding. Formerly, a yeast two-hybrid screen identified an interaction between the second PDZ domain of MAGI-1 (325–577) and RSK1 [16]. We initiated a quantitative characterization of this interaction using purified PDZ protein and a chemically synthesized seven amino acid long RSK1 peptide. Unexpectedly, a fluorescence polarization-based protein-peptide-binding assay could not be used to measure PDZ-RSK1 peptide binding as no change in the fluorescence polarization signal (or fluorescence intensity) was detected when PDZ domain concentration was increased in the presence of fixed amount of labeled RSK1 peptides (712–735 or 729–735) (Fig. 3A). However, this does not prove that the protein and the labeled peptide fail to interact, as the N-terminal fluorescent group may remain highly uncoordinated even if the PDZ domain binds to the C terminus of the peptide. Therefore, microscale thermophoresis (MST) was used and a ~ 20 μM interaction was detected (Fig. 3B). With competitive titration experiments, we could also show that phosphorylation at the major C-terminal autophosphorylation site (Ser732) does not influence the steady-state-binding affinity of the CTT peptide (729–735) to the second PDZ domain of MAGI-1 (Fig. 3C).

Phosphorylation at Ser732 affects ERK2-RSK1 (CTT) binding

RSK1 binds to ERK2 with a MAPK-binding linear motif located in the CTT. Interestingly, ERK2-binding affinity to the RSK1 peptide decreased five-fold (from 0.2 μM to 1 μM) when the peptide was phosphorylated at Ser732 (Fig. 3D). This five-fold affinity decrease was further confirmed using two different CTT peptide lengths (Fig. 3E,F), and a similar decrease in affinity was observed in the presence of an excess (100 μM) of MAGI-1 PDZ domain (Fig. 3H). Because of the lack of any fluorescence anisotropy change upon PDZ binding, we were also able to measure the binding affinity of ERK2 to RSK1 CTT in the presence of large amount of MAGI-1 PDZ domain (Fig. 3G). Interestingly, PDZ domain binding affected ERK2-RSK1 CTT affinity only moderately indicating that a ternary complex can form between the MAPK, MAPKAPK, and a PDZ domain containing substrate (Fig. 3I).

The crystal structure of the ERK2-RSK1(CTT) protein–peptide complex had been formerly determined [10,15,27]. However, the C-terminal region following the MAPK docking motif was disordered (729–735) in that structure (Fig. 1C), preventing the observation of possible contacts between the autophosphorylatable Ser732 and the ERK2 interaction surface. Nonetheless, we observed here that Ser732 phosphorylation lowered ERK2-RSK1(CTT)-binding affinity. Therefore, we reasoned that some extra residues outside of the MAPK linear motif may play a role in ERK–RSK binding. Unrestrained FlexPepDock simulations [28] were used to investigate the potential conformations of the ERK2 bound state (Fig. 4A). This *ab initio* modeling suggested that ERK2 bound CTT may mediate an additional contact via Lys729. To validate this putative interaction *in vitro*, the ERK2-binding affinity of a truncated RSK1 peptide containing only the core of the MAPK-binding linear motif (which is visible in the crystal structure of the protein–peptide

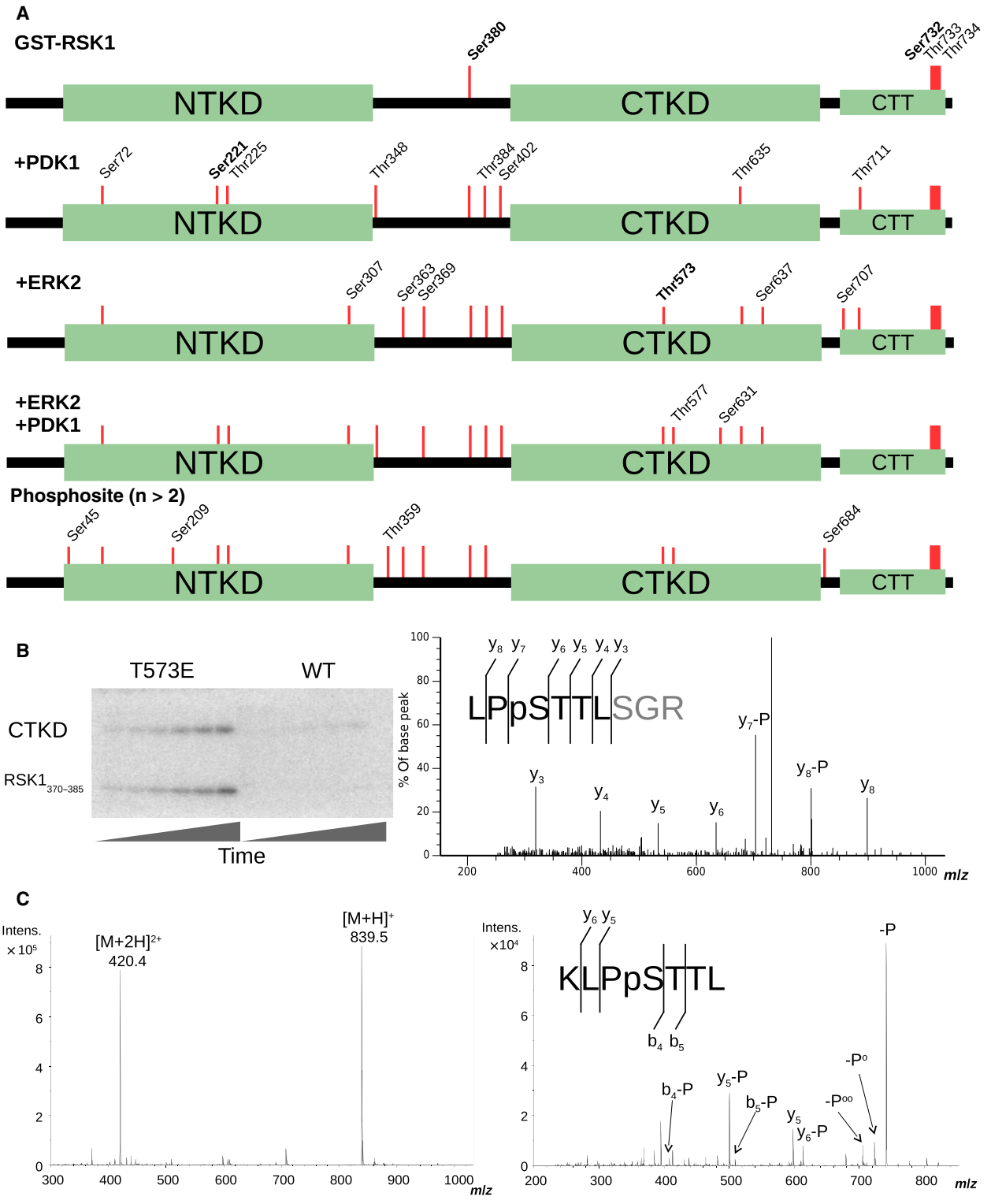

complex) was measured. As expected, the binding strength decreased (more than seven-fold) (Fig. 4B). Moreover, replacing Lys729 with alanine (K729A) generated a comparable decrease in binding affinity, while an alanine substitution at Ser732 did not affect ERK2 binding (Fig. 4C).

In conclusion, Lys729 is likely involved in a transient interaction in the ERK2 bound state, which was invisible in the crystal structure. In phosphorylated CTT, Lys729 may interact with the phosphate group via electrostatic interactions. This intramolecular charge clamp would prevent the formation of a presumably transient interaction between the CTT and ERK2 and will lead to weakened binding [11].

Crystal structure solution of RSK1 CTT peptide–MAGI-1 PDZ domain complexes

In order to structurally characterize RSK CTT and PDZ domain binding, we set out to determine the high-resolution structure of the RSK1 peptide–MAGI-1 PDZ domain complex by X-ray crystallography. As expected, the bound RSK1 peptide shows a canonical class I PDZ domain-binding mode (Fig. 5A) [29]. The PDZ ligand peptide adopts an antiparallel β-sheet conformation and mediates several main chain directed interactions augmenting the β2 strand of the PDZ domain. The C-terminal Leu735 fits into the hydrophobic pocket of the PDZ domain, Thr734 (at position −1) does not mediate interaction, while Thr733 (at position −2) faces toward His530 creating the canonical hydrogen bond interaction of class I PDZ ligands [29]. Ser732 is also in hydrogen bond distance (2.9 Å) to Lys499.

The C terminus of human papillomavirus (HPV) E6 interacts with a set of tumor suppressor proteins such as MAGI-1, and the structure of this PDZ-peptide ligand complex had been formerly reported [30,31]. X-ray structure solution revealed that the E6 peptide and the RSK1 peptide studied herein display a similar core-binding mode (Fig. 5A). The main interaction is mediated by (a) the C-terminal Leu forming main chain-specific bonds as well as hydrophobic contacts; (b) a Thr residue at position −2 forming a hydrogen bond with His530 from the PDZ domain; (c) a side chain–specific hydrogen bond between the hydroxyl group of the Ser at −3 position and Lys499 of MAGI-1. The HPV E6 peptide was reported to bind with greater affinity to the MAGI-1 PDZ domain ($K_D \sim 1$ μM) compared with the RSK1 peptide. This could be best explained by the fact that E6 mediates more extensive contacts, which are additional to the core interactions typical for class I peptides [31].

We also solved crystal structures with phosphorylated CTT peptides (pSer732) and captured the MAGI-1–pRSK1 (CTT) complex in two slightly different crystal forms (Fig. 5B). The phospho-serine rotamer was different between the two crystal structures, although both conformations were compatible with the pSer732-Lys499 hydrogen bond (2.7–3.5 Å) since the lysine side chain rotamer also changed (Fig. 5B). In summary, the CTT phosphorylation at Ser732 is compatible with PDZ binding, while phosphorylation at Thr733 would very likely disrupt RSK1–PDZ (MAGI-1) binding due to steric hindrance within the binding pocket.

Experimental evidence for the intramolecular charge clamp in phosphorylated CTT

Next, we used isothermal calorimetry (ITC) for the biophysical characterization of the binding of the C-terminal RSK1 peptide (CTT) to the PDZ domain from MAGI-1 (Fig. 6). Unexpectedly, this type of analysis suggested that the structure of the CTT may greatly change upon phosphorylation. First, the thermodynamic parameters of complex formation with $RSK1_{696–735}$ or $RSK1_{729–735}$ and with their phosphorylated Ser732 forms were analyzed at 37 °C (Fig. 6A). The parameters of the native RSK1 peptide binding were comparable to that of HPV E6 peptide binding to the same PDZ construct [32]. In contrast to this moderately exothermic binding, the longer phosphorylated peptide showed an endothermic reaction under the same temperature. Moreover, the seven-residue-long $RSK1_{729–73}$ phospho-peptide also showed exothermic binding. In order to investigate this discrepancy and to eliminate a possible experimental artifact, we repeated

Fig. 2. RSK1 phosphopeptide mapping and characterization of autophosphorylation at the C-terminal tail. (A) RSK1 or its ERK2 and PDK1 activated form was analyzed with mass spectrometry. The identified phosphosites are highlighted with red labels for each sample. Sites essential in RSK1 activation are marked in bold. The mock sample contained CTKD autophosphorylation sites (380, 732, 733, 735) because of the weak intrinsic activity of unphosphorylated CTKD. Due to the presence of Ser380 phosphorylation, the PDK1-treated sample contained most of the phosphopeptides also identified from the ERK2 + PDK1-treated sample (CTKD, PDK1, and NTKD phosphosites) except for the ERK2 phosphorylation sites (i.e. 307, 369, 573, 637). The identified *in vitro* phosphorylation sites show a good match with the phosphorylation pattern yielded from high throughput data [24]. Only those Ser/Thr phosphorylation sites are highlighted which were identified in more than two independent high throughput analysis. (B) *Cis* autophosphorylation of the constitutive active CTKD. We observed strong autophosphorylation in an *in vitro* kinase assay (left). The C-terminal peptide phosphorylated on Ser732 was found in the trypsin digested active CTKD HPLC-MS/MS spectra (right). (C) ESI-MS spectrum (left) of the tryptic fragment (KLPSTTL) from the *trans* phosphorylated $RSK1_{696–735}$ substrate peptide. ESI-MS/MS spectrum (right) of the singly charged ion from the phosphorylated peptide: KLPSTTL. -P stands for neutral loss of phosphoric acid, ° label is used for 18 (H_2O) loss.

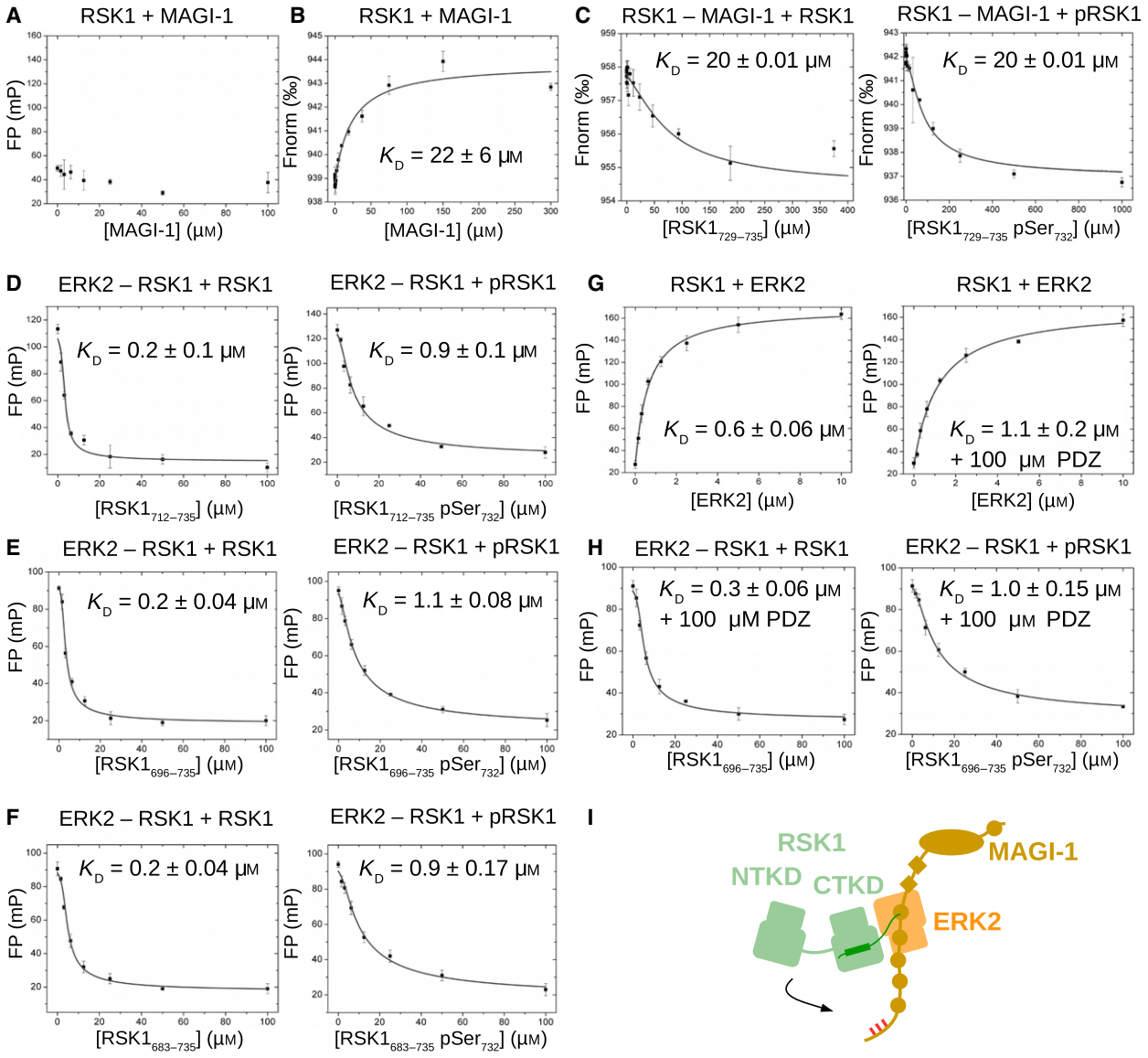

Fig. 3. Biochemical characterization of the effect of Ser732 phosphorylation on RSK1 mediated protein–protein interactions. (A) Fluorescence polarization of the RSK1 peptide does not change upon association with the second PDZ domain of MAGI-1. (B) Thermophoresis of fluorescently labeled RSK1$_{729–735}$ increases upon association with the same PDZ domain. (C) In competitive binding experiments, unlabeled RSK1$_{729–735}$ was used to compete with the binding between the fluorescently labeled RSK1 peptide and the PDZ domain, confirming the binding affinity of the interaction as determined in Panel B. (D) Phosphorylation at 732 affects ERK2 binding. Results of fluorescence polarization-based experiments with unphosphorylated (left panel) and phosphorylated (right panel) RSK1$_{712–735}$ peptide. (E) Competitive binding measurements with a native or phosphorylated RSK1$_{696–735}$ peptide. (F) Competitive binding measurements with a native or phosphorylated RSK1$_{683–735}$ peptide. (G) Direct FP measurements between ERK2 and RSK1$_{712–735}$ in the absence (left) and the presence of 100 μM PDZ domain (right). (H) Analysis of ternary complex formation between ERK2, RSK1$_{696–735}$ peptide, and MAGI-1 PDZ domain. The left panel shows ERK2 binding with the native peptide and the right panel shows binding with the phosphorylated peptide in the presence of 100 μM MAGI-1 PDZ domain. (I) Schematic representation of the ternary complex between ERK2-RSK1 and MAGI-1. Error bars show SD (n = 3).

the experiment with another phosphopeptide of an intermediate length (RSK1$_{712–735}$) (Fig. 6A). Similarly to RSK1$_{696–735}$, this latter phosphopeptide also showed endothermic binding. We also noticed that the binding affinity decreased parallel to the decrease in peptide length. The small differences in the thermodynamic parameters of the seven-residue-long peptides indicate that phosphorylation at the RSK1 C terminus itself

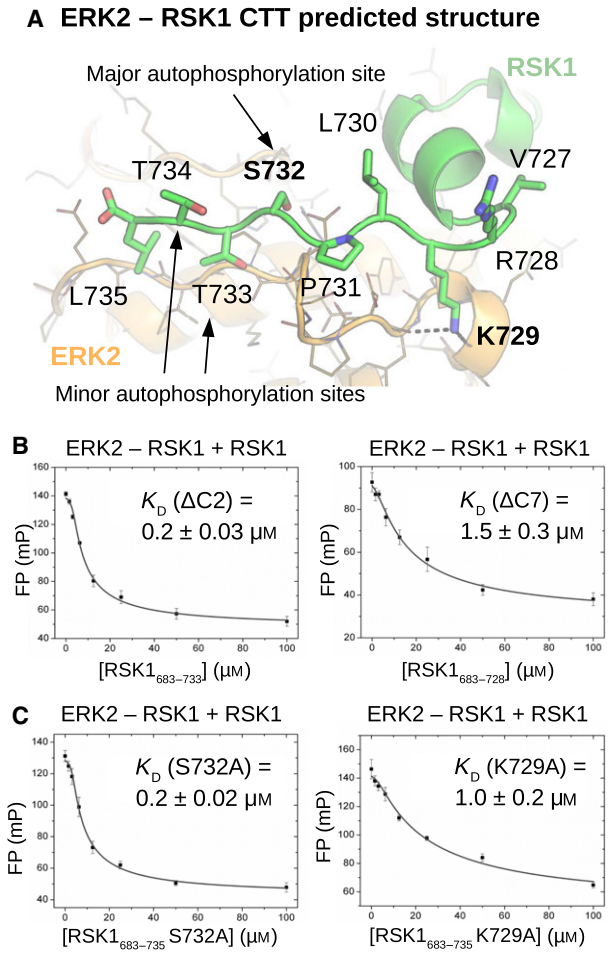

Fig. 4. Characterization of the ERK2–CTT interaction. (A) As the C-terminal tail was not visible in the crystal structures of the ERK2–RSK1(CTKD) and the ERK2–pepRSK1 complexes [10,15,27], we used FlexPepDock simulations to gain insight into the role of the flexible C-terminal part of CTT in ERK2–RSK1 binding. Unrestrained docking calculations from three independent starting structures were performed where the core interacting motif was derived from the protein-peptide crystal structure with an artificially built elongated C terminus. We found that the top calculations showed both dissociated and associated tails from the ERK2 docking surface. Lys729 was coordinated by the main chain of ERK2 in the cluster of associated tails (~ 50% of the calculated models). (B) Competitive binding measurements with the $RSK1_{683–733}$ and $RSK1_{683–723}$ peptides. The peptide lacking the two utmost C-terminal residues (ΔC2) bound similarly to MAPKs as the wild-type but the peptide devoid of a longer C-terminal region (ΔC7) showed decreased binding, despite that this latter peptide lacked all residues that were visible in the ERK2–RSK1 docking peptide crystallographic complex. (C) Competitive binding measurements with the S732A and K729A $RSK1_{683–735}$ peptides. Single-point mutation of Lys729 can mimic the effect of Ser732 phosphorylation. The Ala substitution of Ser732 does not affect MAPK binding directly. Error bars show SD (n = 3).

does not influence interaction with the MAGI-1 PDZ domain, confirming conclusions derived from the crystallographic analysis. However, the endothermic nature of binding between the PDZ domain and the longer $RSK1_{712–735}$ (or $RSK1_{696–735}$) peptide suggests that some degree of disordered-to-order transition occurs in the CTT upon phosphorylation. This local fold would likely be remodeled upon PDZ binding. A positively charged region of the MAPK-binding region is required for binding at the common docking (CD) groove of MAPKs [15]. As this region lies just next to the RSK1 autophosphorylation site, it is likely that the phosphorylated residues make electrostatic contacts to docking motif residues and thus affect PDZ and MAPK binding.

Based on ITC measurements, ΔH showed linear decrease with increasing temperature, indicating that the signal is specific to peptide binding and is not biased by other temperature-dependent events such as thermal denaturation (Fig. 6B). The change of heat capacity (ΔC_p) was estimated as the slope of a linear fit to the determined ΔH values between 10C and 37 °C (Fig. 6). ΔC_p is mainly proportional to changes in hydration upon binding [33]. Decrease in ΔC_p indicates more extensive solvent exposed hydrophobic surface burial upon complex formation. Binding studies with the E6 peptide and the same PDZ construct showed that ΔC_p increases (becomes less negative) if interactions outside the core motif or the core PDZ domain cannot form [32]. Because there is similar amount of amino acid burial in the minimal E6-PDZ and in the unphosphorylated $RSK_{729–735}$–PDZ complex, they both display a similar ΔC_p value (-150 cal·mol^{-1}·K^{-1}) (Fig. 6B, table, rows 5 and 1, respectively). This finding indicates that the native RSK1 peptide interacts only through its core motif and the binding does not induce any conformational change in the MAGI-1 PDZ domain. ΔC_p can also be calculated from protein–peptide structures, and this structure-based calculation (considering the core interacting residues) showed a good agreement with the ΔC_p of PDZ binding measured for the unphosphorylated and the phosphorylated $RSK1_{729–735}$ peptides (Fig. 6B, table, rows 1 and 3, respectively). In contrast, comparison of the measured ΔC_p values of a longer peptide ($RSK_{712–735}$) to that of the shorter $RSK_{729–735}$ peptide and differences in this value caused by phosphorylation (Fig. 6B, table, rows 1–3) suggest that there are intramolecular interactions in the free phosphorylated form of the longer ($RSK_{712–735}$) peptide, which are absent in the shorter phosphopeptide. Lys729 could not be solely responsible for this effect

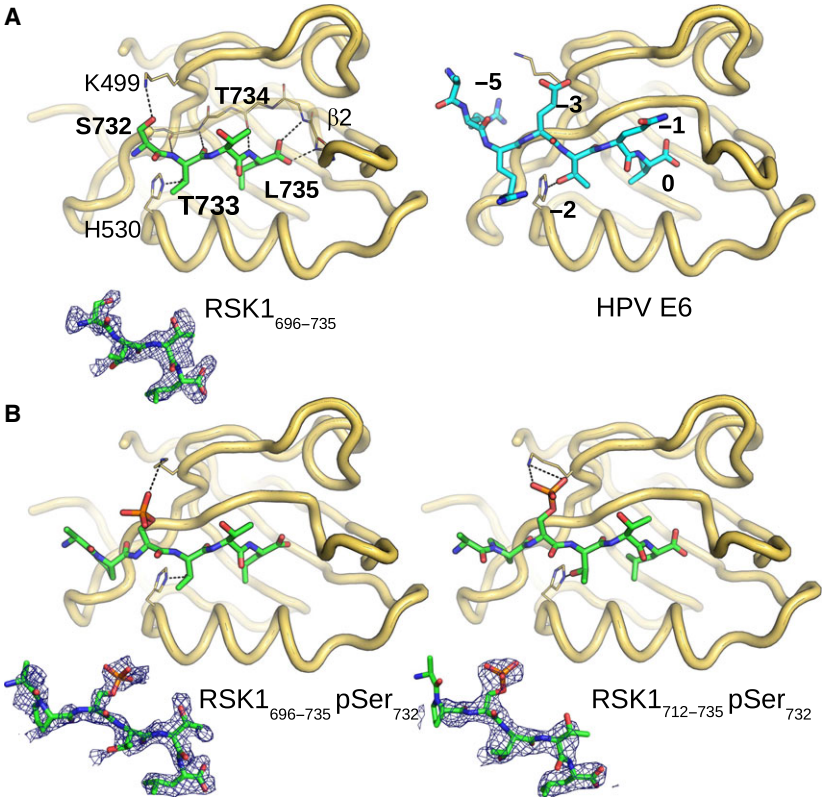

Fig. 5. Crystal structure of MAGI-1 PDZ domain complexed with the native and phosphorylated RSK1 peptides. (A) RSK1 CTT binds as a class I PDZ peptide. The panel shows the comparison with the PDZ-HPV E6 peptide ligand structure [31]. (B) Upon phosphorylation at the Ser residue at position −3 (Ser732), the RSK1 peptide mediates different side chain–specific interactions with Lys499 from MAGI-1. This interaction was captured in two different rotamers in two different crystal forms, which shows that Lys499 follows the rotation of the phosphoryl group. The phospho-mimicking Glu of E6 at position −3 does not mediate interaction with MAGI-1 [32] . The lower insets show feature-enhanced maps contoured at 2 σ around the bound peptides. The second PDZ domain of MAGI-1, RSK1, and E6 peptides is shown in yellow, green, and cyan, respectively.

because calculated and measured ΔC_p values matched to the shorter peptide. Conversely, based on the discrepancy between calculated and measured ΔC_p values for the longer peptide, one can estimate the hydration of the intramolecularly shielded residues, which is 60–70 cal·mol^{-1}·K^{-1} suggesting that it is a small intramolecular clamp, possibly involving residues N-terminal to Lys729.

CTT structural dynamics in solution

In order to gain structural insights into the intramolecular clamp formed in the phosphorylated CTT, we applied NMR spectroscopy to characterize the native or phosphorylated CTT conformations and PDZ bound states in solution. The phosphorylated long RSK1 CTT peptide (696–735) was produced by CTKD phosphorylation *in vitro*. Changes in the ^{1}H-^{15}N HSQC spectra of RSK1$_{696–735}$ peptides confirmed that autophosphorylation by CTKD occurred only at Ser732 (Fig. 7A). Despite phosphorylation, the secondary structure propensities remain highly similar compared to the unphosphorylated peptide and chemical shift mapping showed that Ser732 phosphorylation affected only the proximal residues (Fig. 7B). Secondary chemical shifts (SCS) data demonstrated that the MAPK-binding linear motif region displays helical propensity, which is in good agreement with our previous observations [10]. Upon complex formation with the PDZ domain, the core interaction motif (the last five residues) became invisible in the NMR spectrum as a result of signal broadening confirming their central role in complex formation (Fig. 7C,D).

Prolyl *cis-trans* isomerization is frequently found in disordered protein regions, not only in structured domains [34]. Usually minor peaks can be observed for *cis*-Pro surrounding residues (with ~ 10% intensity compared to the corresponding major *trans*-peak) (Fig. 7E). In the case of the unphosphorylated peptide, such minor peaks can be assigned to Leu730 and Ser732, which are next to *cis*-Pro731. In contrast, a considerably longer minor fragment (between residues 728–735) became apparent in the NMR spectrum of the phosphorylated peptide (Fig. 7F). This region showed large beta propensity based on SCS values. Interestingly, the minor peak of Lys729 displayed similarly large chemical shift deviation upon phosphorylation as that of Ser732. Overall, this NMR data indicated significant chemical shift changes for residues of the charged motif (Arg725, Arg726, Arg728, and Lys729). Pro731 undergoes *cis-trans* isomerization and the chemical shift differences for Lys729 and Arg728

A

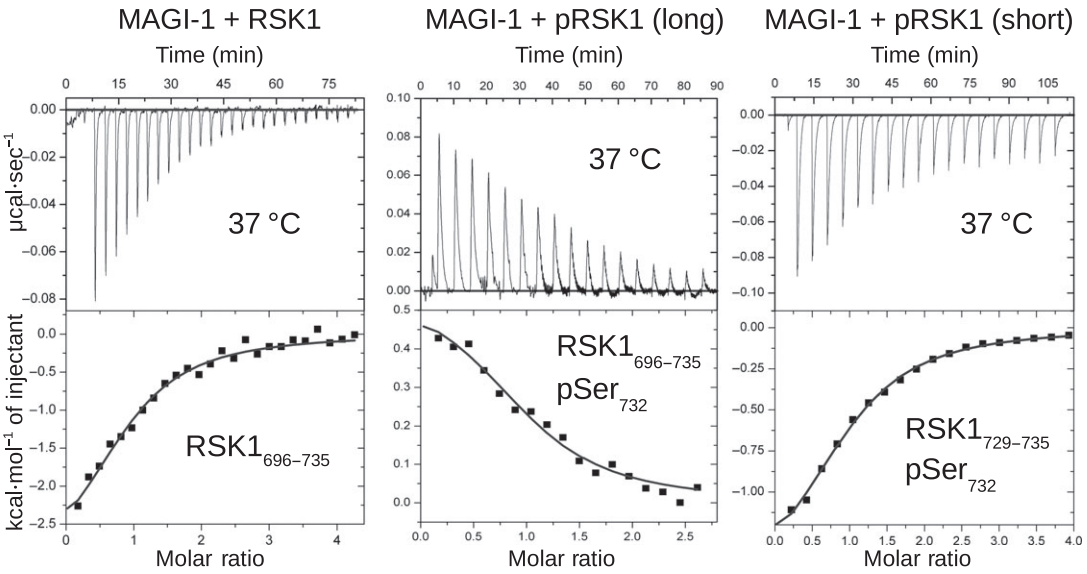

Peptide	T (°C)	K_D (µM)	N (sites)	ΔH (kcal·mol^{-1})	ΔS (cal·mol^{-1}·K^{-1})	$-T\Delta S$ (kcal·mol^{-1})
$RSK1_{696–735}$	37	12.6 ± 2.5	0.92 ± 0.08	–3.35 ± 0.35	11.6	–3.60
$RSK1_{696–735}$ $pSer_{732}$	37	14.2 ± 4.0	1.01 ± 0.06	0.57 ± 0.04	24.0	–7.44
$RSK1_{712–735}pSer_{732}$	37	27.4 ± 4.7	1.13 ± 0.04	0.76 ± 0.04	23.3	–7.22
	30	34.0 ± 6.1	1.18 ± 0.05	1.29 ± 0.08	24.7	–7.48
	20	45.9 ± 4.1	1.03 ± 0.03	2.22 ± 0.10	27.4	–8.03
	10	71.4 ± 8.2	0.88 ± 0.05	3.13 ± 0.27	30.0	–8.49
$RSK1_{729–735}$	37	38.6 ± 2.3	1.01 ± 0.02	–2.49 ± 0.07	12.2	–3.78
	30	32.6 ± 1.9	1.08 ± 0.02	–1.27 ± 0.03	16.3	–4.94
	20	42.7 ± 2.9	1.31 ± 0.23	0.22 ± 0.06	20.7	–6.07
	10	46.9 ± 2.8	0.88 ± 0.02	1.79 ± 0.06	26.1	–7.39
$RSK1_{729–735}$ $pSer_{732}$	37	37.7 ± 2.0	0.95 ± 0.03	–1.67 ± 0.08	14.8	–4.59
	30	37.5 ± 2.9	1.29 ± 0.03	–0.69 ± 0.02	18.0	–5.45
	20	26.3 ± 7.3	0.77 ± 0.06	0.50 ± 0.05	22.7	–6.65
	10	53.7 ± 8.8	0.49 ± 0.08	2.34 ± 0.43	27.8	–7.87

B

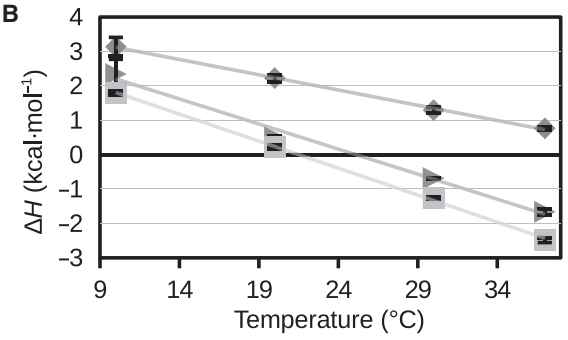

	Peptide	ΔC_p (cal·mol^{-1}·K^{-1})	Calculated ΔC_p (cal·mol^{-1}·K^{-1})
1	$RSK1_{729–735}$	–157.0 ± 3.1	–167.9
2	$RSK1_{712–735}$ $pSer_{732}$	–88.5 ± 2.4	–143.9
3	$RSK1_{729–735}$ $pSer_{732}$	–145.8 ± 10	–143.9
4	E6 to MAGI-1	–470 ± 45*	
5	E6 to core MAGI-1	–150 ± 20*	

Fig. 6. Thermodynamic impact of RSK1 phosphorylation at Ser732 on PDZ binding. (A) Characterization of MAGI-1 PDZ–RSK1 peptide interactions by ITC. The results of titration experiments at 37 °C between the PDZ domain of MAGI-1 and a native or two phosphorylated RSK1 peptides. The table below summarizes the results of similar experiments at 10, 20, and 30 °C. (B) ΔC_p was estimated as the slope of the temperature dependence of ΔH as measured by ITC. Determined heat capacity changes are listed in the table on the right, where values for E6 were obtained from Ref. [32]. Note that ΔC_p values obtained for RSK1 and E6 peptides are directly comparable as they were all determined using the same PDZ construct of MAGI-1. Asterisk indicates ΔC_p values that were taken from Ref. [32].

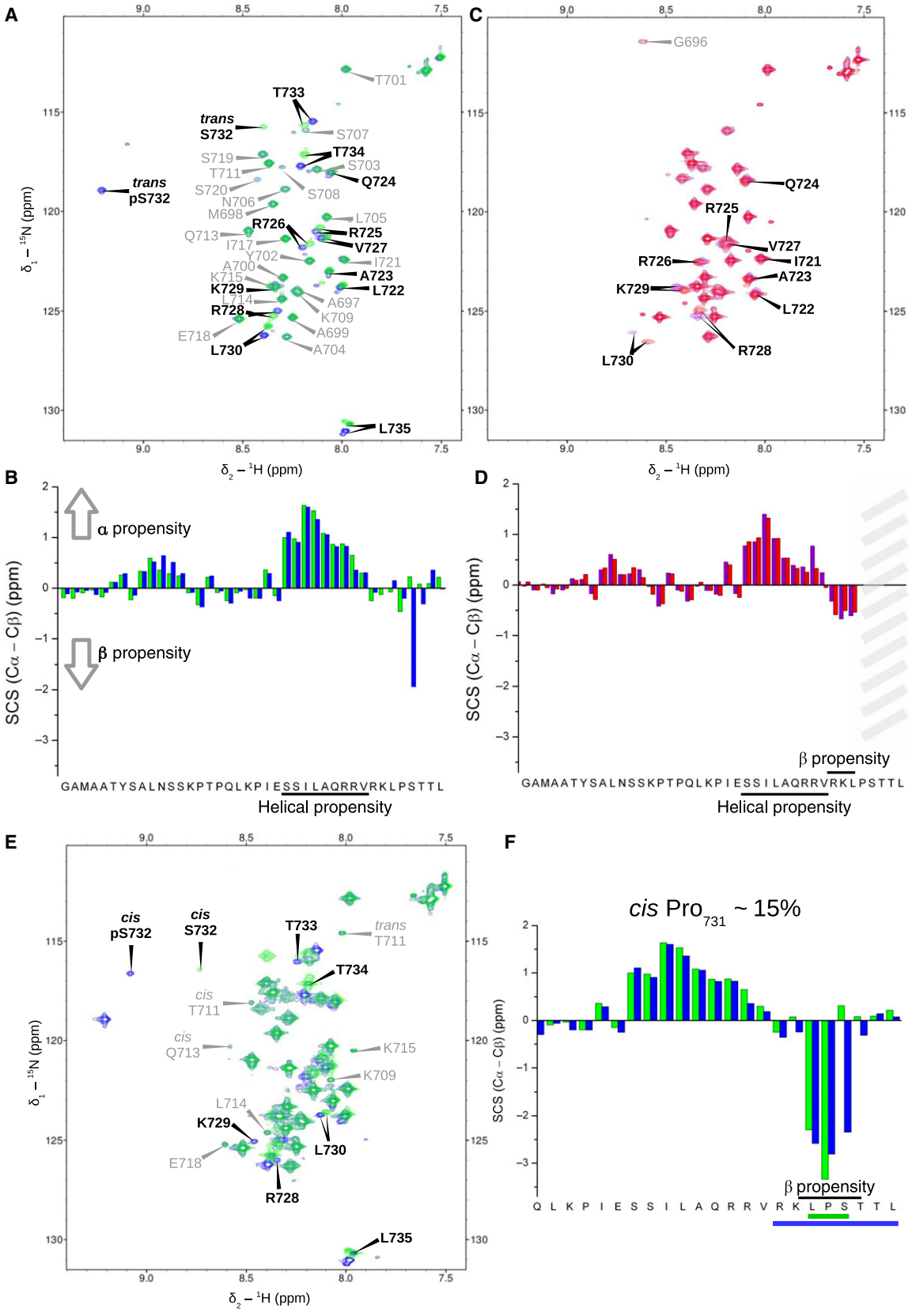
A
C
B
D
E
F
δ1 – 15N (ppm)
δ2 – 1H (ppm)
trans pS732
trans S732
T733
T734
Q724
R725
R726
V727
A723
K729
L722
R728
L730
L735
cis pS732
cis S732
cis T711
cis Q713
trans T711
α propensity
β propensity
SCS (Cα – Cβ) (ppm)
GAMAATYSALNSSKPTPQLKPIESSILAQRRVRKLPSTTL
Helical propensity
cis Pro731 ~ 15%

are more prominent in the *cis*-Pro peptide, suggesting the existence of a more pronounced charge clamp specifically involving these latter two residues.

Next, molecular dynamics (MD) simulations were used to further address the conformational dynamics of the CTT in different states. These computations also indicated the existence of conformationally distinct charge clamps in the CTT (Fig. 8A). Various charge clamp interactions were found in either the *trans*- or *cis*-Pro731 peptides (Fig. 9). MD trajectories showed that, despite that these interactions are dynamic, the negative charge of the phospho-residue could efficiently mask the MAPK binding charged motif. *Cis*-Pro can be considered as the core of type VI group β-turns and the stabilization of this β-turn conformation by phosphorylation is the likely reason why a larger *cis*-Pro containing minor fragment in the NMR data could be identified (Fig. 8B).

Real-time monitoring of protein–protein interactions in living cells after EGF stimulation

After structural and biochemical characterization, we set out to address the impact of CTT autophosphorylation in living cells. We were particularly interested in the dynamics of the protein–protein interactions that RSK1 mediates with its partners (ERK2 and MAGI-1). Protein–protein interactions can be detected in cells by multiple methods; however, many of these lack the possibility of monitoring transient interactions as the reporter system significantly alters their behavior. A recent technique involving a novel split luciferase, called NanoBiT, was developed to monitor dynamic protein–protein association events in cells [35] (Fig. 10A). This protein-fragment complementation assay includes two fragments: an 11-residue-long peptide fragment and a 18-kDa large fragment. We cloned RSK1 with the N-terminal peptide fragment and the other interaction partners with the large fragment attached to either their N or C terminus. We also made a single C-terminal residue-truncated RSK1 (ΔC1) incapable of PDZ binding, a mutant deficient in MAP kinase binding (L714E), and two other mutants, in which residues constituting the phosphorylation-dependent charge clamp were mutated (S732A and K729A) (Fig. 10B).

We found that the ERK2–RSK1 interaction was unaffected by ΔC1, but it was significantly reduced for the L714E mutant as expected (Fig. 10C). We also monitored the MAGI-1–RSK1 interaction using the same technique. This interaction was decreased greatly by the C-terminal truncation (ΔC1), but it was unaffected by the other mutation designed to probe MAPK binding (Fig. 10G). Interestingly, S732A and K729A mutations did not affect RSK1–MAGI-1 binding, while their association to ERK2 was greatly reduced. Next, we analyzed the effect of epidermal growth factor (EGF) on the ERK2–RSK1 and RSK1–MAGI-1 complexes in live cells (Fig. 10D,H). Interestingly, EGF stimulation caused a moderate disassembly of the RSK1–MAGI-1 complex (~ 30% at the maximum), which was intact in the case of the K729A mutant (Fig. 10I,J).

Upon EGF stimulation, a large drop in luminescence was observed for the ERK2–RSK1 complex, indicating the (partial) disassembly of the complex (Fig. 10E,F). While all mutants displayed some stimulation-induced disassembly, we did not observe as large relative differences for S732A or K729A mutants compared with the wild-type protein, in contrast to an earlier study [11]. However, in that study, co-immunoprecipitation (co-IP) was used to monitor the dynamics of ERK2-RSK1 complex formation requiring cell lysis. This might have led to biased results because weak interactions are less detectable and the co-IP is not reliable if intracellular compartmentalization is an important factor that should be taken into account. Interestingly, some periodicity in the dissociation profiles appeared. Similar periodic kinetics was observed

Fig. 7. NMR analysis on RSK1 CTT peptides: the impact of Ser732 phosphorylation and PDZ binding. (A) ^{1}H-^{15}N HSQC spectra of the free native $RSK1_{696–735}$ peptide (green) and its phosphorylated form (blue). Complete assignment of major peaks is shown. Gray labels show peaks which appear in both spectra with no change. (B) Phosphorylation does not cause large changes in the overall conformation and only affects the neighboring residues of Ser732. The SCS values indicate some helical content in the C-terminal half of the MAPK docking motif. (C) ^{1}H-^{15}N HSQC spectra of the PDZ bound native $RSK1_{696–735}$ peptide (purple) and its phosphorylated form (red). Assignment of shifted peaks is shown. (D) Similarly to the changes caused by phosphorylation for the free peptide, there was no large conformation change in the peptide conformation and only small chemical shifts were observed for the terminal residues. The last four residues which are directly involved in PDZ binding became undetectable. Interestingly, the SCS values for residues neighboring the PDZ-binding region display a beta propensity, which may be the consequence of the clear beta conformation observed for the core motif in the protein-peptide crystal structure. (E) ^{1}H-^{15}N HSQC spectra of the free native $RSK1_{696–735}$ peptide (green) and its phosphorylated form (blue) showed with a lower cut-off compared to panel A. The assignment of minor peaks belonging to cis-Pro peptide conformations is indicated. The isomeric state of Pro residues is highlighted for Pro+1 residues. Gray labels show minor peaks which appear in both spectra without any change. (F) Analysis of the observed chemical shifts in the *cis*-Pro731 RSK1 CTT peptide. The sequence is underlined to indicate which residues showed clear minor peaks, for which the chemical environment changed upon prolyl isomerization.

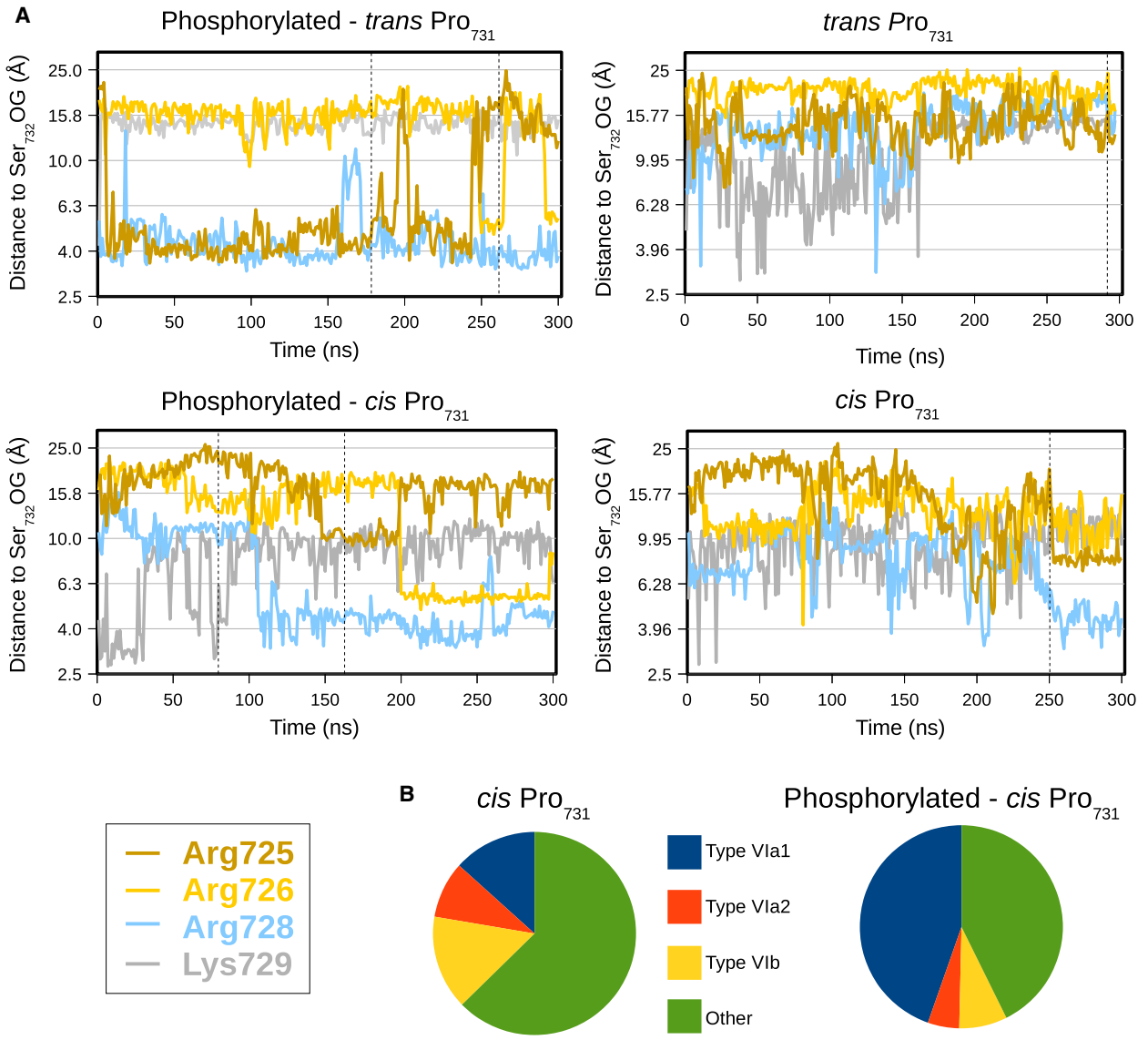

Fig. 8. Molecular dynamics simulation results on the unphosphorylated RSK1 CTT. (A) MD simulation trajectories of the phosphorylated or native CTT peptides (712–735) in *trans* and *cis* conformations. Distances between the four basic residues of the charged motif (NZ and CZ atoms of Arg725, dark orange; Arg726, light orange; Lys729, gray; and Arg728, light blue) and the Ser732 (OG atom) are plotted along the MD trajectory. The frames which were chosen for further display and depict typical CTT structures on Fig. 9 are indicated in the corresponding trajectories by lines. (B) β-Turn analysis based on Φ_{i+1} angles of the MD trajectories of the *cis* conformations. The probability of each type VI turns is showed in a pie chart. Phosphorylation greatly increases the VIa1 conformation.

Fig. 9. Ser732 phosphorylation induces conformational change of the RSK1 C terminus. (A) Normalized amide chemical shift changes upon phosphorylation in the MAPK and PDZ-binding region of the free RSK1 peptide as determined by NMR spectroscopy. (B) The same analysis considering *cis*-Pro731 conformation (if available). (C,D,E,F) Analysis of the 300-ns-long CTT peptide (712–735) MD simulations in *trans* and *cis* conformations, respectively. Arg728(CZ) or Lys729(NZ) or Arg726(CZ) or Arg725(CZ) and the Ser732 (OG atom) distances were calculated along the MD trajectory (in each ns) and were plotted in histograms. The histogram of the native RSK1 peptide is green and the histogram of its phosphorylated form is blue. The insets display typical stable charge clamp conformations. Note that for Arg728, its distance to Ser732 is shifted to lower values in both the cis and trans Pro731 phosphorylated peptide, while for K729, its distance to Ser732 is reduced specifically only in the phosphorylated cis Pro731 peptide. The insets in panel F display typical unphosphorylated peptide conformations.

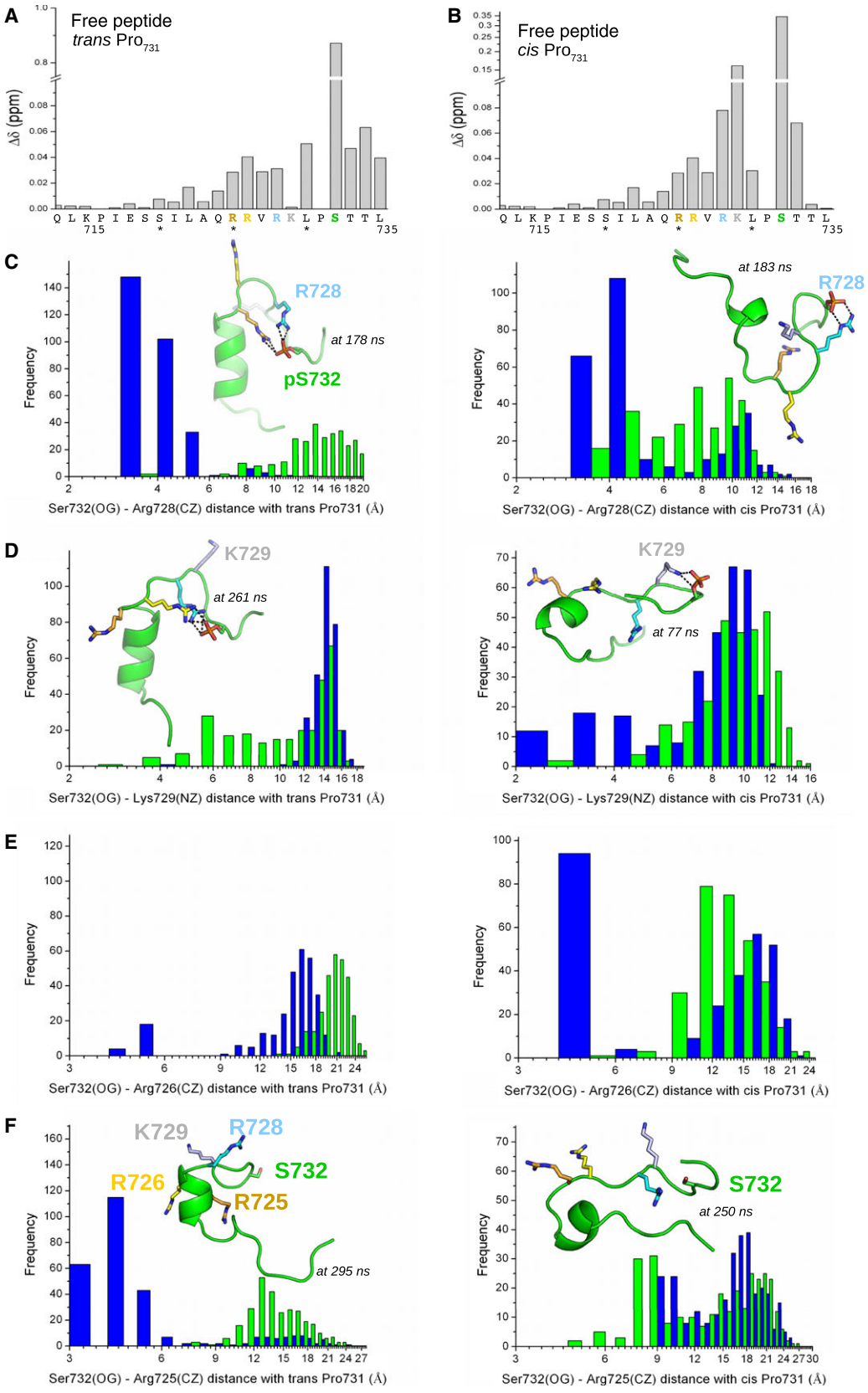
A
Free peptide
trans Pro731
Δδ (ppm)
Q L K P I E S S I L A Q R R V R K L P S T T L
715
735
B
Free peptide
cis Pro731
C
R728
at 178 ns
pS732
Frequency
Ser732(OG) - Arg728(CZ) distance with trans Pro731 (Å)
at 183 ns
R728
Ser732(OG) - Arg728(CZ) distance with cis Pro731 (Å)
D
K729
at 261 ns
Ser732(OG) - Lys729(NZ) distance with trans Pro731 (Å)
K729
at 77 ns
Ser732(OG) - Lys729(NZ) distance with cis Pro731 (Å)
E
Ser732(OG) - Arg726(CZ) distance with trans Pro731 (Å)
Ser732(OG) - Arg726(CZ) distance with cis Pro731 (Å)
F
K729
R728
S732
R726
R725
at 295 ns
Ser732(OG) - Arg725(CZ) distance with trans Pro731 (Å)
S732
at 250 ns
Ser732(OG) - Arg725(CZ) distance with cis Pro731 (Å)

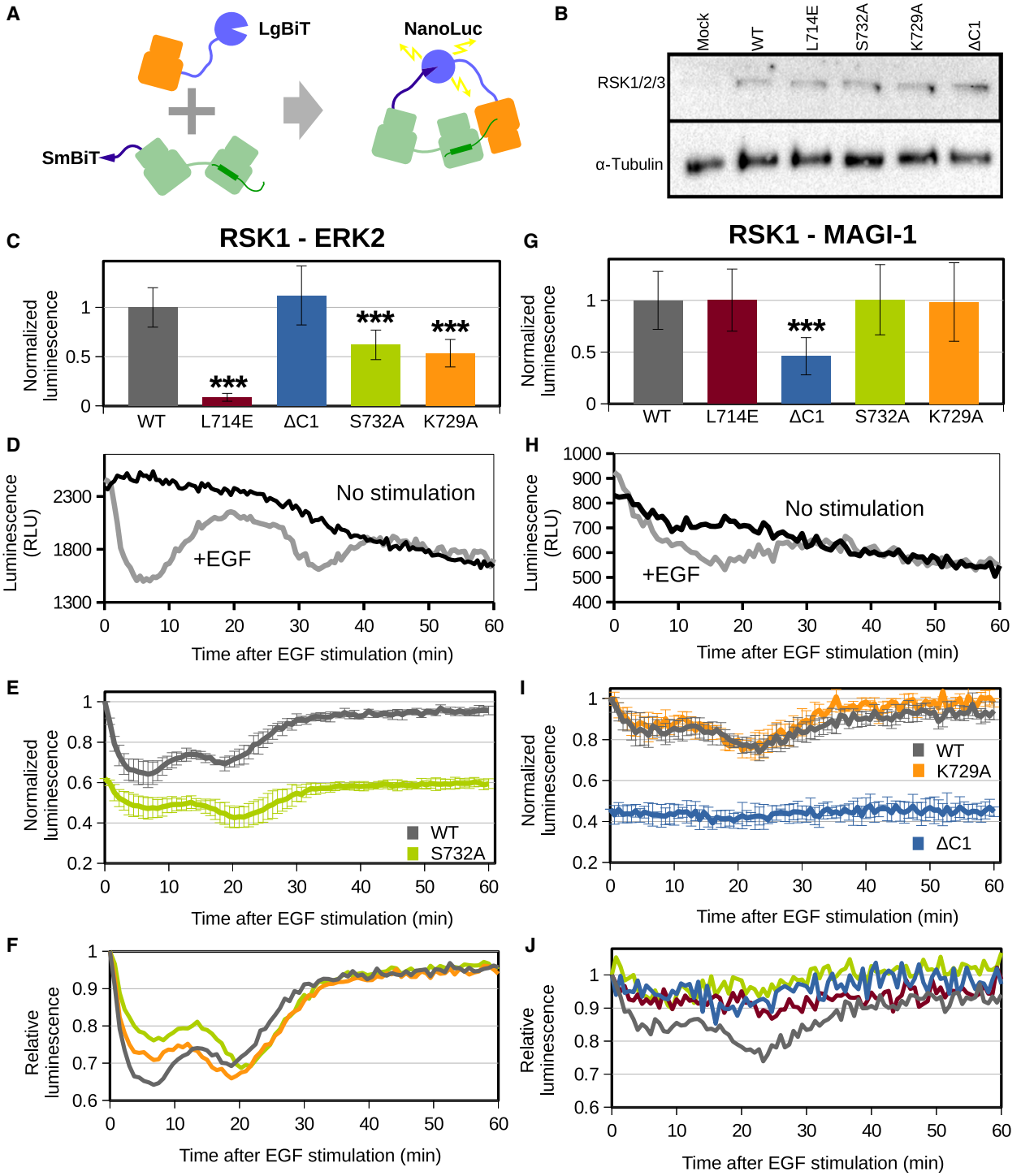

in ERK nuclear translocation [6]. Overall, this result suggests that stimulation-induced translocation may also have an impact on complex disassembly. Nevertheless, S732A and K729A mutants displayed a lower dynamic response.

Modulation of RSK and ERK cellular trafficking upon growth factor stimulation

After establishing that CTT autophosphorylation affects the dynamics of RSK-partner protein binding,

Fig. 10. Dynamic monitoring of RSK1 mediated protein–protein interactions upon EGF stimulation in living cells. (A) Schematic representation of the split NanoLuc (or NanoBiT) experiment. The N terminus of RSK1 was tagged with SmBiT and the interaction partner was tagged with LgBiT in HEK293T cells. After the interaction occurs, the NanoLuc enzyme will be formed and the enzyme activity can be measured in the form of luminescence. (B) A representative western blot of SmBiT tagged RSK1 transfection. Transfection efficiency of different RSK1 mutant constructs was similar. (C) Luminescence signals of ERK2 interactions with different RSK1 mutants in unstimulated HEK293T cells as determined by the NanoBiT complementation assay. Values are normalized to luminescence of the wild-type protein. Error bars show SD ($n \geq 9$). (D) Impact of EGF stimulation on the ERK2-RSK1 complex. Upon EGF stimulation (100 ng·mL^{-1}), the initial signal decreased and then increased indicating a dynamic assembly. (E) Measured luminescence was normalized to an averaged signal decay of unstimulated samples. The relative luminescence change of S732A has lower amplitude and displays less dynamics. Error bars show SD ($n = 3$). (F) The mean of the relative luminescence signal for the native and mutant RSK1 complexes with ERK2. The alteration of the charge clamp mechanism modulates the dissociation kinetics of the complex after EGF stimulation. (G) Luminescence signals of MAGI-1 interaction with different RSK1 mutants in resting cells. Luminescence is normalized to the signal of the wild-type protein. Error bars show SD ($n = 6$). (H) Impact of EGF stimulation on the RSK1–MAGI-1 complex. (I) The normalized luminescence signal shows that MAGI-1 dissociation is unaffected by the K729A mutation, but it is highly dependent on the presence of the PDZ-binding motif. (J) The mean of the relative luminescence signal for the native and mutant RSK1 complexes with MAGI-1 ($n = 4$). Error bars show SD ($n = 3$). Asterisks indicate statistical significance (***$P < 0.001$) calculated by two-tailed Student's *t*-test.

we wanted to address how these observed dynamic changes relate to the proteins' movement between cellular compartments. For example, it is well known that ERK2 displays nuclear translocation upon EGF stimulation [6,36]. We wanted to test whether RSK undergoes similar translocation or not. Endogenously expressed pan-RSK (RSK1/2/3) and pan-ERK (ERK1/2) were monitored in parallel experiments upon EGF stimulation using immunofluorescence (Fig. 11A). We found that both proteins shift toward the nucleus upon stimulation with a highly similar time profile (Fig. 11B). Next, the specific localization of the phosphorylated kinase species was examined using an anti-phospho RSK antibody developed against pSer380 and an anti-phospho ERK antibody developed against double phosphorylated pThr202/pTyr204. According to our results, pERK localized similarly to pan-ERK, but we also observed strong localization at the centrosomes during metaphase (Figs 11C and 12) [37]. In contrast, pRSK localized strictly in the cytoplasm, whereas pan-RSK translocated mostly to the nucleus upon stimulation. These differences in the translocation trends of ERK and RSK show that they move independently during their activation and highlight the dynamically regulated nature of this signaling complex (Fig. 11D).

Discussion

Monitoring protein–protein interactions in cells revealed dynamic changes in the assembly of ERK pathway-related signaling complexes

How protein phosphorylation mechanistically contributes to the emergence of dynamic signaling complex assembly is not well-explored. By using a protein–protein interaction assay, which was specifically designed to allow the detection of dynamic protein–protein associations in living cells [35], we monitored RSK1–ERK2 or RSK1–MAGI-1 binding and showed that RSK1 complex formation dynamically changes following EGF stimulation. The time between the ERK2–RSK1 dissociation spikes was ~ 12–25 min, and the spikes had a rapid rise time (~ 6 min) and a slower decay time (≥ 9 min). Earlier, a similar oscillation profile for nuclear ERK shuttling or ERK phosphorylation was reported upon EGF stimulation [6]. In another work, similar but more sustained oscillation (with a mean periodicity of ~ 100 min) was found after FGF stimulation in phosphorylated ERK or Ras-GTP levels [38]. The current model behind this periodic pattern under sustained stimulation postulates a negative feedback at an upstream level triggered by activated ERK. The observed independent localization trends of activated ERK and activated RSK (Fig. 11D) and the charge clamp-based dissociation promoting effect of RSK1 CTT (Fig. 10F) can synergistically contribute to the periodicity and the amplitude of macroscopically observed pERK dissociation patterns. In addition, RSK phosphorylation (and probably nuclear localization) may also display an ERK-like periodic pattern because of its observed dynamic dissociation from MAGI-1. In summary, we found that the earlier reported dynamic pattern of ERK nuclear shuttling and activation shows an interesting agreement to the dynamics of some ERK controlled protein–protein complex formation events measured in our study. Thus, complex dynamic properties such as oscillations may already be apparent at the level of physical interactions between key components of the ERK pathway.

Oscillatory Ras/ERK activity, although its function remains enigmatic, has been proposed to be a novel

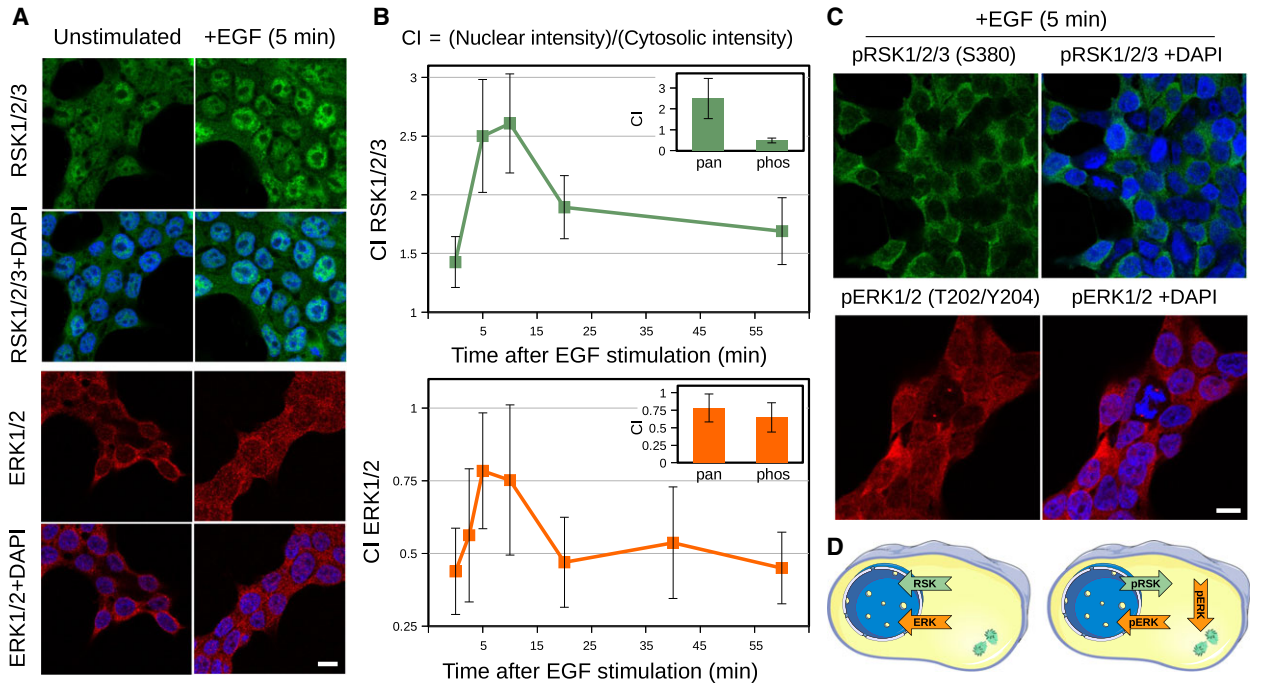

Fig. 11. Mitogen stimulation induces differential translocation of activated ERK and RSK. (A) Translocation of endogenous RSK1/2/3 or ERK1/2 upon EGF stimulation (100 ng·mL^{-1}) in HEK293T cells as determined by immunofluorescence and confocal microscopy. (B) Time course of the translocation. Intensities for cell index (CI) calculations were integrated in identical areas. Error bars show SD (n = 50). The insets show the CI at 5 minutes after EGF stimulation for signals obtained by using pan-ERK, pan-RSK and phospho-ERK, phospho-RSK antibodies. (C) Localization of phosphorylated RSK1/2/3 and ERK1/2 in EGF-stimulated (100 ng·mL^{-1}, 5 min) HEK293T cells. Scale bars represent 10 μm. (D) Schematic model of ERK and RSK translocation during EGF stimulation. The panel was adapted from Servier Medical Art. The cell nucleus was stained with the fluorescent dye DAPI.

molecular clock [38]. In addition, rapid biochemical oscillations, which do not require transcriptional level feedback, may be a means to selectively turn on a subset of genes controlled by the ERK pathway [39]. Similarly, the functional significance of the observed dynamic dissociation–association patterns remains to be elucidated. Nevertheless, our study provides the first glimpse on the way protein complex formation is dynamically regulated by a MAP kinase.

Classification of linear motif-based phosphoswitches

The CTT of RSK has several autophosphorylation sites. We found that the C-terminal autophosphorylation site of RSK1 is mainly Ser732, but the adjacent Thr residues may also be phosphorylated (Fig. 2). RSK1 activation has a negative feedback on specific PDZ mediated interactions by directly interfering with the core motif. Interestingly, phosphorylation of Ser732 participates in the formation of a charged clamp, which affects ERK–RSK binding.

Surprisingly, most of the phosphorylation sites identified in proteins do not have a dedicated role and cannot be considered as a regulatory switch [1,5]. Nevertheless, phosphorylation, as a major post-translational regulatory mechanism, does trigger changes in the structure of proteins in various ways. A dominant class of switches induces intramolecular conformational changes. A well-known example for this group is the activation loop of a kinase domain, which is disordered in the unphosphorylated state but gets ordered after phosphorylation, and then turns on the activity of the kinase domain. Phosphorylation can also trigger extreme changes in the global fold compared with simple loop remodeling as described above [40]. Interestingly, phosphorylation in or near linear-binding motifs located in disordered protein regions may achieve its effect by locally influencing the ability of a functional site to interact with a structured domain. Mechanistically, these linear motif-based phosphoswitches fall into different classes (Fig. 13). There are simple ON and OFF switches and ON and OFF dimmers. For SH2 domains, Tyr phosphorylation is essential for peptide binding, thus an SH2 domain

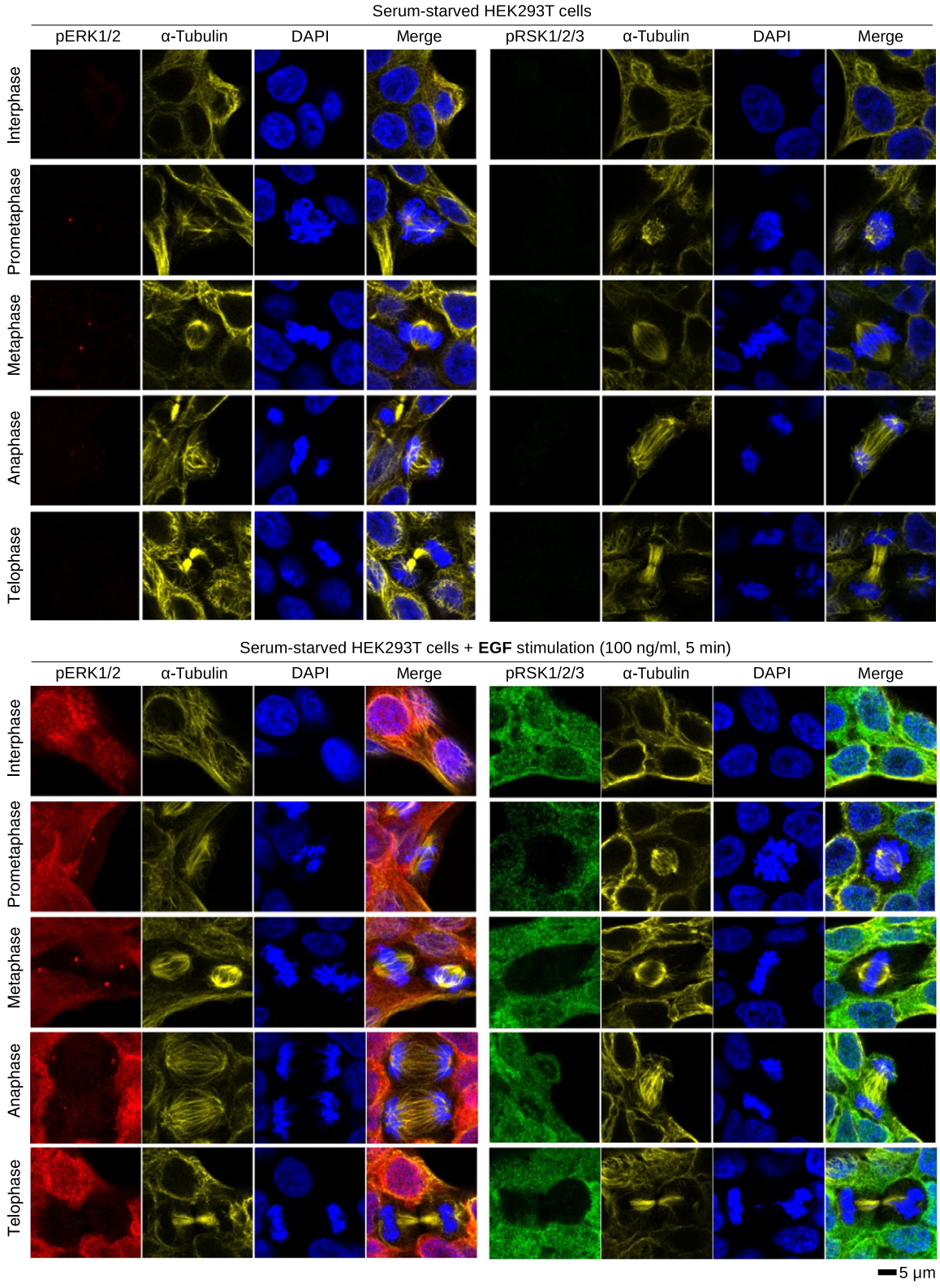

Fig. 12. Intracellular localization of phosphorylated ERK and RSK during mitosis. Serum-starved or EGF-stimulated HEK cells stained with DAPI (nuclear stain), anti-α-tubulin, and anti-phospho antibodies. Phosphorylated ERK localizes at the centrosomes during early metaphase and disappears during anaphase. Both phosphorylated ERK and RSK are present in lower amounts during cell division.

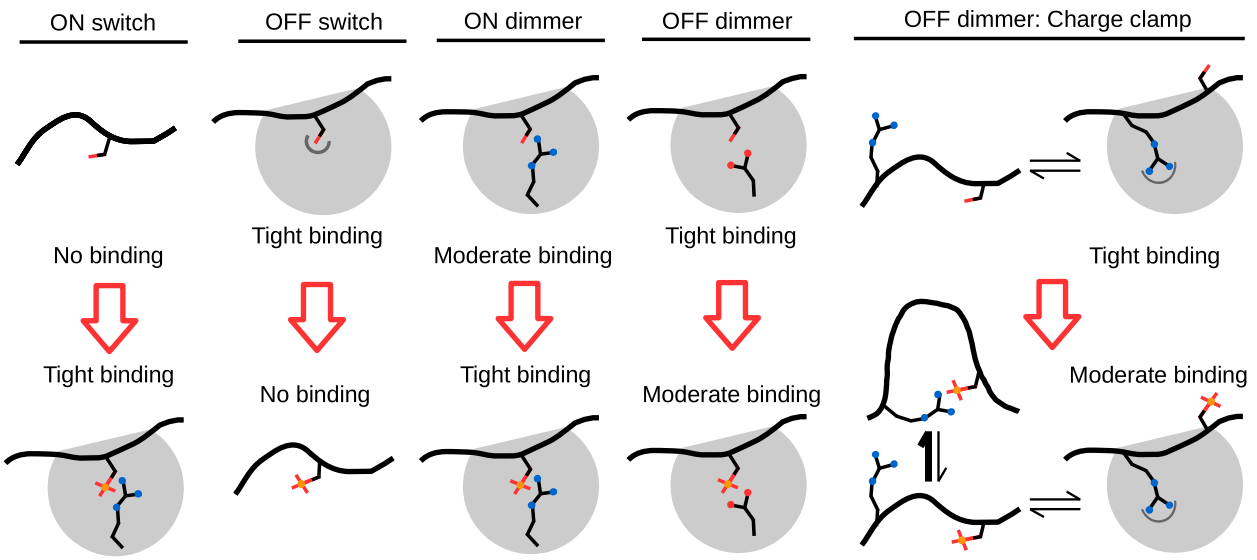

Fig. 13. Classification of linear motif-based switches modulated by phosphorylation. In case of a classical phosphoswitch, phosphorylation alters the binding properties of the linear motif. There are ON and OFF switches and ON and OFF dimmers. For the latter, changes in binding affinity are less dramatic and dimmers only adjust the interaction strength, where phosphorylation either increases it (ON) or dampens it (OFF). Charge clamps have a similar effect as OFF dimmers, but they achieve their dampening effect via a distinct mechanism, which is more indirect compared to that of classical dimmers. Phosphorylation mediates intramolecular interactions in their free disordered state, which then represents a kinetic barrier for their binding to interaction partners.

ligand may be regarded as an ON switch. In contrast, dimmers only adjust the interaction strength and can be considered as modulators. The PDZ domain of SNX27 binds to class I PDZ targets, where phosphorylation of position −2 disrupts the core interaction (OFF switch), whereas phosphorylation of either position −3, −5, or −6 increases the binding affinity by introducing new interactions (ON dimmer) [41]. OFF dimmers decrease binding affinity via intermolecular repulsion [42]. Other OFF dimmers may work mechanistically differently; they introduce an additional conformational selection step into the process of partner binding by using a charge clamp. Here, the phosphorylation triggers a transient local fold that can result in slowed-down conformational kinetics [43]. Similar intramolecular charge clamps have already been shown in some cases [44–46]; however, the RSK1 CTT phosphoswitch appears to be the first clear case where it acts as a modulator on the assembly of a signaling complex. Since a conserved cluster of basic residues is a hallmark feature of nuclear localization signals or AGC kinase substrate motifs [24], the functionality of these linear motifs involved in nuclear transport or AGC protein kinase-mediated phosphorylation, respectively, may also be modulated by adjacent phosphorylation sites.

Dynamic regulation is essential in maintaining the specificity and efficiency of signaling pathways [47]. Here, we explored the mechanism underlying RSK C-terminal autophosphorylation and its role in affecting RSK1–ERK2 and RSK1–PDZ complexes. We found that the key element in these dynamically controlled association events is a disordered protein region, which is located outside the structured kinase domains of RSK1. The interaction of phosphorylated residues with positively charged residues in intrinsically disordered regions is likely to be a common mechanism of phosphoregulation. Moreover, linear motif-based phosphoswitches as described here may be frequently used, not only in kinase-substrates networks but also in other protein–protein interaction networks.

Experimental procedures

Protein expression and purification

All protein constructs were expressed in *Escherichia coli* Rosetta(DE3) pLysS (Novagen, Kenilworth, NJ, USA) cells with standard techniques. The expression and purification of ERK2 and the second PDZ domain of MAGI-1 are described in Refs [48] and [15]. Briefly, ERK2 was expressed with an N-terminal cleavable hexahistidine tag which was removed after affinity purification. MAGI-1 was expressed with a TEV cleavable N-terminal hexahistidine-MBP fusion tag. After Ni- and MBP-affinity purification, the reaction mixture was reloaded onto Ni-agarose and the

flow-through was further purified on a Superdex 75 (GE Healthcare, Little Chalfont, UK) gel filtration column. Unphosphorylated RSK1 peptides (696–735 or 370–385) were produced as formerly described in Ref. [13]. For NMR experiments, the ^{15}N- and ^{13}C-labeled peptide was produced similarly, but before induction cells were transferred to $^{15}NH_4Cl$- and ^{13}C D-glucose containing minimal medium. The C-terminal kinase domain of RSK1 (residues 411–735), the full-length RSK1 and PDK1 (residues 50–359) were expressed as N-terminal GST fusion proteins with a C-terminal noncleavable hexahistidine tag. We introduced a phospho-mimicking mutation (T573E) at the activation loop which activated the kinase domain. The $RSK1_{729–735}$ peptide, the Ser phosphorylated, or its fluorescently labeled versions were all chemically synthesized on an automated PSE Peptide Synthesizer (Protein Technologies, Tucson, AZ, USA) with Fmoc strategy. Phosphorylated $RSK1_{712–735}$ peptide was purchased from Thermo Scientific (Waltham, MA, USA). Protein (and Tyr containing peptide); concentrations were determined by UV spectroscopy. For peptides that lacked any aromatic residue, we directly measured their dry mass.

A chimeric PDZ domain-annexin A2 protein was cloned with a removable N-terminal hexahistidine tag into a modified pET15 expression plasmid. TEV protease cleavage leaves an extra GSM linker at the N terminus of the PDZ domain. The construct contained the second PDZ domain of MAGI-1 (455–558) connected by a two amino acid long 'GS' linker to the core annexin A2 domain (ANXA2, 22–339). This fusion protein was expressed using an auto-induction-based protein expression method. The produced protein was purified on Ni-agarose beads, and the affinity tag was cleaved off by TEV protease cleavage. The protein was further purified on an SP ion exchange column at pH 6.5 using a linear gradient from 20 mM NaCl to 1 M NaCl in the presence of 2 mM TCEP. The final sample was eluted at ~ 20% and was concentrated to 330 μM concentration. Crystallization samples were supplemented with 2 mM TCEP, 10% glycerol and 2 mM $CaCl_2$ before the aliquots were frozen in liquid nitrogen.

Kinase reactions

For phosphopeptide mapping, 3 μM GST-RSK1 in the presence or absence of 3 μM GST-PDK1 and 1 μM activated ERK2 was incubated at 32 °C for 1 h with 250 μM ATP. The mixture was separated by SDS/PAGE and the protein band corresponding to RSK1 was cut from the gel for MS studies. Gel slices were treated based on Ref. [49]. *In vitro* phosphorylation of $RSK1_{(370–385)}$ was carried out with CTKD or with the T573E mutant CTKD in the presence of 250 μM ATP and ~ 5 μCi of [γ-^{32}P] ATP. Reactions were stopped with protein loading sample buffer complemented with 20 mM EDTA, boiled and then subjected to SDS/PAGE. The gel was dried and then analyzed by phosphorimaging on a Typhoon Trio+ scanner (GE Healthcare). Sample preparation for MS of the T573E mutant CTKD was identical with the previously described method.

In vitro phosphorylation of unlabeled or ^{15}N- and ^{13}C-labeled RSK1 peptides (100–150 μM) were carried out in the presence of the constitutively active CTKD (5 μM), 1 mM ATP, 5 mM $MgCl_2$, and 1 mM TCEP at 37 °C for 3 h. Phosphorylated peptides were purified by HPLC on a C5 reversed-phase column.

Phosphopeptide mapping and mass spectrometry

Protein sample characterization was performed using a Maxis II ETD QqTOF instrument (Bruker Daltonics, Billerica, MA, USA) coupled to an Ultimate 3000 nanoRSLC system (Dionex, Sunnyvale, CA, USA) under the control of HYSTAR v.3.2 (Bruker Daltonics). Samples were dissolved in 12 μL of 2% acetonitrile and 0.1% formic acid; 3 μL sample was injected onto an Acclaim PepMap100 C-18 trap column (100 μm × 20 mm; Thermo Scientific). Peptides were separated on an ACQUITY UPLC M-Class Peptide BEH C18 column (130 Å, 1.7 μm, 75 μm × 250 mm; Waters, Milford, MA, USA). Raw data were recalibrated using the COMPASS DATAANALYSIS software 4.3 (Bruker Daltonics). Samples were matched with the RSK1 sequence using the MASCOT server v.2.5 (Matrix Science, Boston, MA, USA. The parameters for the Mascot search were set as follows: trypsin digestion where maximum two missed cleavages were allowed and cysteine carbamidomethylation as fixed and oxidation (M), deamidation (NQ), and phosphorylation (ST) as variable modifications. Precursor tolerance was set to 7 ppm, the MS/MS tolerance was 0.05 Da.

ESI-MS measurements of isolated peptides were carried out on a Bruker Daltonics Esquire 3000plus ion trap mass spectrometer using direct sample infusion or online HPLC coupling. For direct analysis, samples were dissolved in 50% acetonitrile and 0.1% acetic acid. HPLC separations were performed on a Jasco PU-2085Plus HPLC system using a Supelco Ascentis C_{18} column (2.1 mm × 150 mm, 3 μm), which was directly coupled to the mass spectrometer. Enzymatic digestion was performed by trypsin (Promega Trypsin Gold, MS grade), using a protein/enzyme ratio of 100 : 1 (w/w) in 10 mM ammonium acetate buffer. In all cases, collision-induced dissociation experiments were used for peptide sequencing.

Binding experiments

Fifty nanomolar reporter peptide ($RSK1_{712–735}$ peptide fluorescein-conjugated at the N terminus) was mixed with increasing amounts of ERK2 or MAGI-1 in fluorescence

polarization (FP)-based titration experiments and the FP signal was measured with a Synergy H4 (BioTek Instruments, Winooski, VT, USA) plate reader in 384-well plates. In competitive FP measurements, 50-nM labeled reporter peptide was mixed with ERK2 in a concentration to achieve ~ 60–80% complex formation. Subsequently, increasing amounts of unlabeled peptide constructs were added. The K_D for each experiment was determined by fitting the data to a quadratic or a competition-binding equation. Titration experiments were carried out in triplicates and the average FP signal was used for fitting the data with ORIGINPRO 7 (OriginLab, Northampton, MA, USA).

Microscale thermophoresis was measured in standard coated capillaries in 20 mM Hepes pH 7.5, 150 mM NaCl, 0.5 mM TCEP, and 0.05% Tween on a Monolith NT.115 instrument (Nanotemper Technologies, München, Germany). We found that the uncleaved MBP fusion protein was more suitable for these measurements than the isolated PDZ domain and the highest signal was achieved by using an N-terminally labeled $RSK1_{729–735}$ peptide as a reporter. In competitive binding experiments, the complex was mixed to achieve near saturation and either unlabeled unphosphorylated or phosphorylated $RSK1_{729–735}$ was used as a competitor. Experiments were performed at 22 °C, 50% LED output, 60% IR-laser power using the fluorescent peptide at constant 50 nM concentration.

Isothermal titration calorimetry (ITC) measurements were carried out in 20 mM Hepes pH 7.5, 150 mM NaCl, and 0.5 mM TCEP using an ITC200 or a VP-ITC apparatus (MicroCal, Worcestershire, UK); 50–100 μM PDZ domain was titrated with 0.8–2 mM RSK1 peptides at 10, 20, 30, or 37 °C. The ORIGIN for ITC 5.0 (OriginLab) software package was used for data processing and data were fitted with a model 'One Set of Sites'. Heat capacity changes ($J \cdot mol^{-1} \cdot K^{-1}$) were calculated based on the empirical formula: $\Delta C_p = 2.14*\Delta ASA_{apol} - 0.88*\Delta ASA_{pol}$, where ΔASA_{apol} and ΔASA_{pol} are the apolar and polar accessible surface area changes ($Å^2$), respectively.

Crystal structure determination of CTT(RSK1)–PDZ(MAGI-1) complexes

To determine the high-resolution structure of the interaction of RSK1 peptide–MAGI-1 PDZ domain, we tried to crystallize the complex at high concentration (> 3–5 mM) using various commercially available crystallization screens. Despite these efforts, no crystals grew and even precipitations were scarce in the crystallization drops. In order to determine the structure of this protein–peptide complex, we tried a carrier-protein-driven crystallization strategy, but instead of using existing fusion tags such as MBP, GST, or thioredoxin, we used the core domain of annexin A2 (ANXA2) [50]. ANXA2 is a calcium-binding perimembrane protein with excellent crystallization properties, good solubility, and stability [51]. The ANXA2-PDZ fusion protein readily crystallized in the presence of C-terminal RSK1 peptides ($RSK1_{696–735}$, $pRSK1_{696–735}$, or $pRSK1_{712–735}$) under various crystallization conditions. Conditions were tested based on previous experience with apo ANXA2. Needle shape crystals grew under various conditions within a few minutes to hours, and the best crystals with the $RSK1_{696–735}$ peptide grew at 8% PEG 4000 in 100 mM acetate buffer at pH 5. Crystals from this condition appeared within a day and gained their maximal size in 3–4 days. Single crystals with different phosphopeptides grew in 14% PEG 8000 and 200 mM $MgCl_2$, in 100 mM TRIS buffer at pH 8.5. Crystals were supplemented with 20% glycerol before flash cooling in liquid nitrogen.

The diffraction datasets were collected on the P14 beamline at EMBL Hamburg and on the PXIII beamline at SLS. The phase problem was solved by molecular replacement with Phaser using PDB entry 1XJL and 2KPK as starting models [31,50,52]. Structure refinement was carried out using PHENIX, and structure remodeling and building were performed in Coot [53,54]. Structure solution revealed two molecules in the asymmetric unit where crystal packing interactions are mainly formed by ANXA2 (Table 1). The short linker (a single Gly-Ser) between the ANXA2 fusion tag and the PDZ domain allowed some flexibility in domain arrangements, but one of the PDZ domains mediated important crystal packing contacts, which stabilized its location in the asymmetric unit. This was apparently important in detecting the RSK1 peptides in the canonical-binding pocket of one of the PDZ domains, while the electron density map around the other PDZ domain remained poorly visible.

NMR measurements

NMR spectra were recorded on a Bruker Avance III 700 spectrometer operating at 700.17 MHz for ^1H, equipped with 5-mm triple-resonance probe head with a *z*-axis gradient. All spectra were measured at 298 K. ^1H chemical shifts were referenced to the internal DSS standard, whereas ^{13}C and ^{15}N chemical shifts were referenced indirectly via the corresponding gyromagnetic ratios. The composition of the samples was as follows: ~ 0.7 mM double-labeled peptide (native or phosphorylated), 20 mM Hepes pH 6.75, 20 mM NaCl, 3 mM NaN_3, 2 mM TCEP, and 10% D_2O. For interaction studies with MAGI-1, the same reaction mixture was supplemented with 1-mM unlabeled PDZ domain. Peak assignment and sequential connectivities were determined from the analysis of BEST-type HNCO, HN(CA)CO, HNCA, HN(CO)CA, HNCACB, HN(CO)CACB measurements. Carbon side-chain chemical shifts were obtained from the CC(CO)NH measurement, important for elucidating the Pro residue isomerization based on the Cβ-Cγ difference. Spectra were processed with TOPSPIN and analyzed using the CARA software [55]. The probability of proline to be in *cis* form was calculated by integration of

Table 1. Crystallographic data collection and refinement statistics

	MAGI-1-ANXA2 in complex with $RSK1_{696–735}$	MAGI-1-ANXA2 in complex with $RSK1_{696–735}$ $pSer_{732}$	MAGI-1-ANXA2 in complex with $RSK1_{729–735}$ $pSer_{732}$
Data collection			
Wavelength (Å)	0.9762	1.0000	1.0000
Space group	C 1 2 1	P 2 2_1 2_1	C 1 2 1
Cell dimensions			
a, *b*, *c* (Å)	195.8, 60.7, 99.7	60.2, 98.6, 200.3	194.9, 60.2, 99.4
α, β, γ (°)	90.0, 98.8, 90.0	90.0, 90.0, 90.0	90.0, 98.7, 90.0
Resolution range (Å)	49.27–2.30 (2.36–2.30)	49.73–2.30 (2.36–2.30)	49.10–2.95 (3.03–2.95)
$CC_{1/2}$	99.9 (77.3)	99.9 (53.3)	99.0 (38.9)
R_{merge}[a]	10.5 (129.0)	21.3 (104.8)	24.7 (83.3)
$<I/\sigma(I)>$	18.03 (2.36)	15.42 (3.00)	8.36 (2.49)
Completeness (%)	100.0 (100.0)	100.0 (100.0)	99.9 (100.0)
Redundancy	12.82 (8.12)	19.87 (18.67)	6.86 (7.21)
No. reflections	51 873 (3854)	53 922 (3925)	24 379 (1785)
Refinement			
R_{work}/R_{free}	0.1906/0.2259	0.1869/0.2401	0.2154/0.2716
No. atoms			
Protein	6495	6632	5900
Ligand/ion	37	45	39
Solvent	220	634	–
B-factors (Å^2)			
Protein	79.60	53.05	40.61
Ligand	70.49	47.79	40.56
Solvent	56.81	43.68	–
Ramachandran			
Favored (%)	96	97	98
Allowed (%)	3.5	2.5	2.0
Outliers (%)	0.5	0.5	0.1
Rotamer outliers (%)	1.9	3.36	1.1
R.m.s deviations			
Bond lengths (Å)	0.002	0.007	0.002
Bond angles (°)	0.523	0.864	0.457
PDB ID	5N7D	5N7F	5N7G

[a] $R_{merge} = \Sigma_{hkl}\Sigma_i|I_i(hkl) - <I(hkl)>|/\Sigma_{hkl}\Sigma_i\ I_i(hkl)$.

HSQC peak intensity. Secondary chemical shift values were determined based on Ref. [56]. Chemical shift variations upon phosphorylation and interaction with the PDZ domain were calculated with the formula: $\Delta\delta = \sqrt{\left(\left(\delta_{H,1} - \delta_{H,2}\right)^2 + \left(0.1 * \left(\delta_{N,1} - \delta_{N,2}\right)^2\right)\right)}$. Assignation of the native and phosphorylated RSK1 peptides were deposited to the BMRB database under the accession codes 27213 and 27214.

Molecular dynamics simulations

All-atom MD simulations were executed with GROMACS, version 5.1.4 program package [57] using AMBER99SB*-ILDNP force field [58] with neutralizing Na^+ counter ions and TIP3 explicit solvent molecules [59]. The length of the unrestrained simulations was 300 ns in all cases. The starting model of trans conformers were created using the MAPK bound conformation (PDB ID: 4NIF) where the invisible C-terminal amino acids were built in an extended conformation. The starting model of *cis* conformers were created similarly, but with a C terminus in a VIa1 β-turn conformation. Peptide *cis* conformation was stable during the whole simulation. The energy-minimized systems were subjected to MD calculations with a time step of 2 fs at a constant temperature of 300 K. The resulting trajectory files were analyzed with programs of the GROMACS package.

Protein–protein interaction assay

The NanoBiT PPI MCS starter system was purchased from Promega (Madison, WI, USA). Full-length RSK1 was cloned into pBit2.1-N[TK/SmBiT] vector. Binding-specific luminescent signal was observed in case of pBit1.1-C[TK/LgBiT]-ERK2 (full-length) and pBit1.1-N[TK/LgBiT]-

MAGI-1 (full-length, cloned from Addgene clone #23523). HEK293T cells were cultured in Dulbecco's modified Eagle's medium (DMEM; Lonza) containing 10% fetal bovine serum and 1% penicillin/streptomycin/amphotericin B. 2×10^4 cells per well were seeded onto a white, TC treated 96-well plate (Greiner, Kremsmünster, Austria) 24 h prior to transfection. Transient transfections were carried out with FuGene HD reagent (Promega) according to the NanoBiT system's instructions. Four hours after transfection, cells were starved for 20 h in CO_2-independent medium (Thermo Scientific). Cells were assayed 24 h after transfection using Nano-Glo reagent (Promega) and a Synergy H4 plate reader (BioTek). Experiments were carried out according to the manufacturer's instructions. Stimulation was performed using 100 $ng \cdot mL^{-1}$ EGF (Sigma-Aldrich, Saint Louis, MO, USA). For detection of transfection efficiency of point mutants, cells were suspended in PBS and samples were subjected to western blot using anti-RSK1/2/3 antibody (1 : 500; CST) and anti-α-tubulin (1 : 5000; Sigma).

Immunofluorescence

For detection of endogenous protein localization, 1×10^5 cells per well were seeded onto a cover slip-containing (Assistent) 24-well plate. Cells were serum-starved prior to EGF stimulation. After stimulation, cells were fixed with 4% PFA solution and blocked for 1 h in 5% BSA and 0.3% Triton-X in PBS at room temperature. Staining of ERK1/2 and RSK1/2/3 was performed using anti-ERK1/2 (1 : 800; CST) and anti-RSK1/2/3 (1 : 100; CST), respectively. Phosphorylated proteins were detected with anti-pRSK pSer380 (1 : 800; CST) or anti-pERKpThr202/pTyr204 (1 : 250; CST). Tubulin staining was performed with anti-α-tubulin (1 : 1000; Sigma). Secondary antibodies were conjugated with Alexa Fluor 647 (anti-rabbit, 1 : 800; Thermo) and Alexa Fluor 488 (anti-mouse, 1 : 500; Thermo). Nuclear staining was performed using DAPI (0.1 $\mu g \cdot mL^{-1}$). After washing, cover glasses were mounted to microscopy slides by Mowiol 4-88 mounting medium (Sigma). Confocal microscopy was carried out using a Zeiss LSM 710 system (Carl Zeiss Microscopy GmbH, Jena, Germany) with a 40× oil objective. Images were processed by the IMAGEJ software.

Acknowledgement

This work was supported by the National Research, Development and Innovation Office (NKFIH) grants: NN114309, K108798 (to AR), K119359 (to LN). The authors thank Gilles Travé for the expression vectors of the MAGI-1 PDZ domain and for the critical reading of the manuscript. We also thank Bence Kiss, Arnold Steckel, Kitti Koprivanacz, Karoly Liliom, and Jozsef Kardos for their help in some of the experiments, as well as Gergely Katona for careful reading of the manuscript. This work has been supported by iNEXT project number 653706, funded by the Horizon 2020 program of the European Union. The authors thank the support of the BAG project MX-378 and the beam line scientist at EMBL Hamburg P13/P14 and PSI SLS PXIII. GG and BBK were supported through the New National Excellence Program of the Hungarian Ministry of Human Capacities. GS acknowledges the support of the János Bolyai Research Scholarship of the Hungarian Academy of Sciences. AR is the recipient of the Momentum Grant from the Hungarian Academy of the Sciences (LP2013-57). We also thank the support of the MedInProt program of the Hungarian Academy of Sciences, the National Development Agency Grant (KMOP-4.2.1/B-10-2011), NVKP_16-1-2016-0037, VEKOP-2.3.3.-15-2016-00011, and FIEK16-1-2016-0005 grants from the National Research, Development and Innovation Office, Hungary.

Conflicts of Interest

There is no conflict of interest.

Author contributions

GG conceived the project, carried out the experiments, analyzed data, and wrote the paper. LN and AR supervised the research, analyzed data, and wrote the paper. BB-K and HV contributed by carrying out cell-based experiments, BS and LB did confocal microscopy, ALP and AA prepared peptide and protein samples for biochemical measurements. AB measured NMR data. GS, AÁ, and LT carried out mass spectrometry measurements.

References

1 Nishi H, Hashimoto K & Panchenko AR (2011) Phosphorylation in protein-protein binding: effect on stability and function. *Structure* **19**, 1807–1815.
2 Pearson G, Robinson F, Gibson TB, Xu B-E, Karandikar M, Berman K & Cobb MH (2001) Mitogen-activated protein (MAP) kinase pathways: regulation and physiological functions. *Endocr Rev* **22**, 153–183.
3 Gould CM, Diella F, Via A, Puntervoll P, Gemünd C, Chabanis-Davidson S, Michael S, Sayadi A, Bryne JC, Chica C *et al.* (2010) ELM: the status of the 2010 eukaryotic linear motif resource. *Nucleic Acids Res* **38**, D167–D180.

4 Peti W & Page R (2013) Molecular basis of MAP kinase regulation. *Protein Sci* **22**, 1698–1710.
5 Pawson T (2004) Specificity in signal transduction: from phosphotyrosine-SH2 domain interactions to complex cellular systems. *Cell* **116**, 191–203.
6 Shankaran H, Ippolito DL, Chrisler WB, Resat H, Bollinger N, Opresko LK & Wiley HS (2009) Rapid and sustained nuclear-cytoplasmic ERK oscillations induced by epidermal growth factor. *Mol Syst Biol* **5**, 332.
7 Kholodenko BN, Hancock JF & Kolch W (2010) Signalling ballet in space and time. *Nat Rev Mol Cell Biol* **11**, 414–426.
8 Cargnello M & Roux PP (2011) Activation and function of the MAPKs and their substrates, the MAPK-activated protein kinases. *Microbiol Mol Biol Rev* **75**, 50–83.
9 Pearce LR, Komander D & Alessi DR (2010) The nuts and bolts of AGC protein kinases. *Nat Rev Mol Cell Biol* **11**, 9–22.
10 Alexa A, Gógl G, Glatz G, Garai Á, Zeke A, Varga J, Dudás E, Jeszenői N, Bodor A, Hetényi C *et al.* (2015) Structural assembly of the signaling competent ERK2–RSK1 heterodimeric protein kinase complex. *Proc Natl Acad Sci U S A* **112**, 2711–2716.
11 Roux PP, Richards SA & Blenis J (2003) Phosphorylation of p90 ribosomal S6 kinase (RSK) regulates extracellular signal-regulated kinase docking and RSK activity. *Mol Cell Biol* **23**, 4796–4804.
12 Dalby KN, Morrice N, Caudwell FB, Avruch J & Cohen P (1998) Identification of regulatory phosphorylation sites in mitogen-activated protein kinase (MAPK)-activated protein kinase-1a/p90. *J Biol Chem* **273**, 1496–1505.
13 Gógl G, Alexa A, Kiss B, Katona G, Kovács M, Bodor A, Reményi A & Nyitray L (2015) Structural basis of Ribosomal S6 Kinase 1 (RSK1) inhibition by S100B Protein: modulation of the Extracellular Signal-regulated Kinase (ERK) signaling cascade in a calcium-dependent way. *J Biol Chem* **291**, 11–27.
14 Malakhova M, Tereshko V, Lee S-Y, Yao K, Cho Y-Y, Bode A & Dong Z (2008) Structural basis for activation of the autoinhibitory C-terminal kinase domain of p90 RSK2. *Nat Struct Mol Biol* **15**, 112–113.
15 Garai Á, Zeke A, Gógl G, Törő I, Ferenc F, Blankenburg H, Bárkai T, Varga J, Alexa A, Emig D *et al.* (2012) Specificity of linear motifs that bind to a common mitogen-activated protein kinase docking groove. *Sci Signal* **5**, ra74.
16 Thomas GM, Rumbaugh GR, Harrar DB & Huganir RL (2005) Ribosomal S6 kinase 2 interacts with and phosphorylates PDZ domain-containing proteins and regulates AMPA receptor transmission. *Proc Natl Acad Sci U S A* **102**, 15006–15011.
17 Cai L, Loo LS, Atlashkin V, Hanson BJ & Hong W (2011) Deficiency of sorting nexin 27 (SNX27) leads to growth retardation and elevated levels of N-methyl-D-aspartate receptor 2C (NR2C). *Mol Cell Biol* **31**, 1734–1747.
18 Lim HC & Jou T-S (2016) Ras-activated RSK1 phosphorylates EBP50 to regulate its nuclear localization and promote cell proliferation. *Oncotarget* **7**, 10283–10296.
19 Moritz A, Li Y, Guo A, Villén J, Wang Y, Macneill J, Sprott K, Zhou J, Possemato A, Ren JM *et al.* (2011) Akt-RSK-S6-kinase signaling networks activated by oncogenic receptor tyrosine kinases. *Sci Signal* **3**, ra56.
20 Zaric J, Joseph J-M, Tercier S, Sengstag T, Ponsonnet L, Delorenzi M & Rüegg C (2012) Identification of MAGI1 as a tumor-suppressor protein induced by cyclooxygenase-2 inhibitors in colorectal cancer cells. *Oncogene* **31**, 48–59.
21 Zhang H, Wang D, Sun H, Hall RA & Yun CC (2007) MAGI-3 regulates LPA-induced activation of Erk and RhoA. *Cell Signal* **19**, 261–268.
22 Yang X, Zheng J, Xiong Y, Shen H, Sun L, Huang Y, Sun C, Li Y & He J (2010) Beta-2 adrenergic receptor mediated ERK activation is regulated by interaction with MAGI-3. *FEBS Lett* **584**, 2207–2212.
23 Tonikian R, Zhang Y, Sazinsky SL, Currell B, Yeh JH, Reva B, Held HA, Appleton BA, Evangelista M, Wu Y *et al.* (2008) A specificity map for the PDZ domain family. *PLoS Biol* **6**, 2043–2059.
24 Hornbeck PV, Zhang B, Murray B, Kornhauser JM, Latham V & Skrzypek E (2015) PhosphoSitePlus, 2014: mutations, PTMs and recalibrations. *Nucleic Acids Res* **43**, D512–D520.
25 Dobrosotskaya I, Guy RK & James GL (1997) MAGI-1, a membrane-associated guanylate kinase with a unique arrangement of protein-protein interaction domains. *J Biol Chem* **272**, 31589–31597.
26 Utepbergenov D, Hennig PM, Derewenda U, Artamonov MV, Somlyo AV & Derewenda ZS (2016) Bacterial expression, purification and in vitro phosphorylation of full-length ribosomal S6 kinase 2 (RSK2). *PLoS One* **11**, 1–17.
27 Gógl G, Törő I & Reményi A (2013) Protein-peptide complex crystallization: a case study on the ERK2 mitogen-activated protein kinase. *Acta Crystallogr D* **69**, 486–489.
28 London N, Raveh B, Cohen E, Fathi G & Schueler-Furman O (2011) Rosetta FlexPepDock web server – high resolution modeling of peptide-protein interactions. *Nucleic Acids Res* **39**, W249–W253.
29 Sheng M & Sala C (2001) PDZ domains and the organization of supramolecular complexes. *Annu Rev Neurosci* **24**, 1–29.
30 Zhang Y, Dasgupta J, Ma RZ, Banks L, Thomas M & Chen XS (2007) Structures of a human papillomavirus

(HPV) E6 polypeptide bound to MAGUK proteins: mechanisms of targeting tumor suppressors by a high-risk HPV oncoprotein. *J Virol* **81**, 3618–3626.
31 Charbonnier S, Nominé Y, Ramírez J, Luck K, Chapelle A, Stote RH, Travé G, Kieffer B & Atkinson RA (2011) The structural and dynamic response of MAGI-1 PDZ1 with noncanonical domain boundaries to the binding of human papillomavirus E6. *J Mol Biol* **406**, 745–763.
32 Ramírez J, Recht R, Charbonnier S, Ennifar E, Atkinson RA, Travé G, Nominé Y & Kieffer B (2015) Disorder-to-order transition of MAGI-1 PDZ1 C-terminal extension upon peptide binding: thermodynamic and dynamic insights. *Biochemistry* **54**, 1327–1337.
33 Gomez J, Hilser VJ, Xie D & Freire E (1995) The heat capacity of proteins. *Proteins* **22**, 404–412.
34 Lu KP, Finn G, Lee HT & Nicholson LK (2007) Prolyl cis-trans isomerization as a molecular timer. *Nat Chem Biol* **3**, 619–629.
35 Dixon AS, Schwinn MK, Hall MP, Zimmerman K, Otto P, Lubben TH, Butler BL, Binkowski BF, MacHleidt T, Kirkland TA *et al.* (2016) NanoLuc complementation reporter optimized for accurate measurement of protein interactions in cells. *ACS Chem Biol* **11**, 400–408.
36 Wainstein E & Seger R (2016) The dynamic subcellular localization of ERK: mechanisms of translocation and role in various organelles. *Curr Opin Cell Biol* **39**, 15–20.
37 Verlhac MH, de Pennart H, Maro B, Cobb MH & Clarke HJ (1993) MAP kinase becomes stably activated at metaphase and is associated with microtubule-organizing centers during meiotic maturation of mouse oocytes. *Dev Biol* **158**, 330–340.
38 Nakayama K, Satoh T, Igari A, Kageyama R & Nishida E (2008) FGF induces oscillations of Hes1 expression and Ras/ERK activation. *Curr Biol* **18**, 332–334.
39 Shankaran H & Wiley HS (2010) Oscillatory dynamics of the extracellular signal-regulated kinase pathway. *Curr Opin Genet Dev* **20**, 650–655.
40 Bah A, Vernon RM, Siddiqui Z, Krzeminski M, Muhandiram R, Zhao C, Sonenberg N, Kay LE & Forman-Kay JD (2015) Folding of an intrinsically disordered protein by phosphorylation as a regulatory switch. *Nature* **519**, 106–109.
41 Clairfeuille T, Mas C, Chan AS, Yang Z, Tello-Lafoz M, Chandra M, Widagdo J, Kerr MC, Paul B, Mérida I *et al.* (2016) A molecular code for endosomal recycling of phosphorylated cargos by the SNX27-retromer complex. *Nat Struct Mol Biol* **23**, 921–932.
42 Sun Q, Jackson RA, Ng C, Guy GR & Sivaraman J (2010) Additional serine/threonine phosphorylation reduces binding affinity but preserves interface topography of substrate proteins to the c-Cbl TKB domain. *PLoS One* **5**, 1–11.
43 Stanley N, Esteban-Martín S & De Fabritiis G (2014) Kinetic modulation of a disordered protein domain by phosphorylation. *Nat Commun* **5**, 5272.
44 Lucrèce M, Emmanuelle S, Fabienne B, Sandrine S, Olivier L & Gérard B (2011) Sequence-dependent enrichment of a model phosphopeptide: a combined MALDI-TOF and NMR study. *Anal Chem* **83**, 3003–3010.
45 Kumar P, Chimenti MS, Pemble H, Schönichen A, Thompson O, Jacobson MP & Wittmann T (2012) Multisite phosphorylation disrupts arginine-glutamate salt bridge networks required for binding of cytoplasmic linker-associated protein 2 (CLASP2) to end-binding protein 1 (EB1). *J Biol Chem* **287**, 17050–17064.
46 Martin EW, Holehouse AS, Grace CR, Hughes A, Pappu RV & Mittag T (2016) Sequence determinants of the conformational properties of an intrinsically disordered protein prior to and upon multisite phosphorylation. *J Am Chem Soc* **138**, 15323–15335.
47 Pouysségur J, Volmat V & Lenormand P (2002) Fidelity and spatio-temporal control in MAP kinase (ERKs) signalling. *Biochem Pharmacol* **64**, 755–763.
48 Charbonnier S, Stier G, Orfanoudakis G, Kieffer B, Atkinson RA & Travé G (2008) Defining the minimal interacting regions of the tight junction protein MAGI-1 and HPV16 E6 oncoprotein for solution structure studies. *Protein Expr Purif* **60**, 64–73.
49 Shevchenko A, Tomas H, Havlis J, Olsen JV & Mann M (2006) In-gel digestion for mass spectrometric characterization of proteins and proteomes. *Nat Protoc* **1**, 2856–2860.
50 Rosengarth A & Luecke H (2004) Annexin A2 – does it induce membrane aggregation by a new multimeric sate of the protein. *Annexins* **1**, e34–e41.
51 Ecsédi P, Kiss B, Gógl G, Radnai L, Buday L, Koprivanacz K, Liliom K, Leveles I, Vértessy B, Jeszenoi N *et al.* (2017) Regulation of the equilibrium between closed and open conformations of annexin A2 by N-terminal phosphorylation and S100A4-binding. *Structure* **25**, 1195–1207.e5.
52 McCoy AJ, Grosse-Kunstleve RW, Adams PD, Winn MD, Storoni LC & Read RJ (2007) Phaser crystallographic software. *J Appl Crystallogr* **40**, 658–674.
53 Adams PD, Afonine PV, Bunkóczi G, Chen VB, Davis IW, Echols N, Headd JJ, Hung L-W, Kapral GJ, Grosse-Kunstleve RW *et al.* (2010) PHENIX: a comprehensive Python-based system for macromolecular structure solution. *Acta Crystallogr D* **66**, 213–221.
54 Emsley P, Lohkamp B, Scott WG & Cowtan K (2010) Features and development of Coot. *Acta Crystallogr D* **66**, 486–501.

55 Keller R (2004) The Computer Aided Resonance Assignment Tutorial. CANTINA Verlag, Goldau.
56 Wishart DS, Bigam CG, Holm A, Hodges RS & Sykes BD (1995) H-1, C-13 and N-15 random coil NMR chemical-shifts of the common amino-acids. 1. Investigations of nearest-neighbor effects. *J Biomol NMR* **5**, 67–81.
57 Pronk S, Páll S, Schulz R, Larsson P, Bjelkmar P, Apostolov R, Shirts MR, Smith JC, Kasson PM, van der Spoel D *et al.* (2013) GROMACS 4.5: a high-throughput and highly parallel open source molecular simulation toolkit. *Bioinformatics* **29**, 845–854.
58 Aliev AE, Kulke M, Khaneja HS, Chudasama V, Sheppard TD & Lanigan RM (2014) Motional timescale predictions by molecular dynamics simulations: case study using proline and hydroxyproline sidechain dynamics. *Proteins* **82**, 195–215.
59 Jorgensen WL, Chandrasekhar J, Madura JD, Impey RW & Klein ML (1983) Comparison of simple potential functions for simulating liquid water. *J Chem Phys* **79**, 926.